Title:

Combinatorial patterns of graded RhoA activation and uniform F-actin depletion promote tissue curvature

Authors: Marlis Denk-Lobnig[1], Natalie C Heer[1], Adam C Martin[1, 2]

---

[1] Biology Department, Massachusetts Institute of Technology, 77 Massachusetts Ave., Cambridge, MA 02139

[2] Corresponding author: acmartin@mit.edu

Abstract

During development, gene expression regulates cell mechanics and shape to sculpt tissues. Epithelial folding proceeds through distinct cell shape changes that occur in different regions of a tissue. Here, using quantitative imaging in *Drosophila melanogaster*, we investigate how patterned cell shape changes promote tissue bending during early embryogenesis. We find that the transcription factors Twist and Snail combinatorially regulate a unique multicellular pattern of junctional F-actin density, which corresponds to whether cells apically constrict, stretch, or maintain their shape. Part of this pattern is a gradient in junctional F-actin and apical myosin-2, and the width of this gradient regulates tissue curvature. The actomyosin gradient results from a gradient in RhoA activation that is refined by a balance between RhoGEF2 and the RhoGAP C-GAP. Thus, cell behavior in the ventral furrow is choreographed by the interplay of distinct gene expression patterns and this coordination regulates tissue shape.

Introduction

During development, the three-dimensional shape of a complex organism is generated, in part, by gene expression patterns that are encoded by a one-dimensional sequence of nucleotides in the genome. Patterns of gene expression and resulting signaling processes overlap and interact in space and time to define each cell's function. For example, morphogen gradients encode positional information for specific cell fates (Rogers and Schier, 2011; Wolpert, 1969). For tissues to obtain their final and functional state, cell fates, shapes, and mechanics all need to be positionally specified. Cell fate and mechanical patterns need not be identical, as mechanical properties are often patterned within cells of the same type (Mongera et al., 2018; Sui et al., 2018; Sumigray et al., 2018). Each tissue shape change requires coordinated changes in cell shape and position across the tissue, which have to be tailored to the tissue's morphological and functional requirements while being robust and reproducible between individual embryos/organisms (Chanet et al., 2017; Hong et al., 2016; von Dassow and Davidson, 2009).

Mesoderm invagination in the early *Drosophila melanogaster* embryo involves folding an epithelial sheet and is an established model system for gene expression patterning and morphogenesis (Leptin, 2005). Mesoderm invagination requires apical constriction, a cell shape change driven by actomyosin constriction that converts columnar epithelial cells to a wedge shape, which promotes tissue bending (Leptin and Grunewald, 1990; Sweeton et al., 1991). Importantly, apical constriction is coordinated across the presumptive mesoderm; there is a spatial, ventral-lateral gradient of apical non-muscle Myosin-2 (myosin) and apical constriction that extends ~ 5 - 6 cell rows from the ventral midline (Heer et al., 2017; Lim et al., 2017; Oda and Tsukita, 2001; Spahn and Reuter, 2013) (Fig. 1 A). Beyond this gradient, apical myosin levels reach a baseline low level, and 2 - 4 cell rows (rows ~ 7 – 9) stretch their apical surface and bend towards the forming furrow (Heer et al., 2017; Leptin and Grunewald, 1990; Sweeton et al., 1991). In contrast, more lateral cells, which are part of the neighboring ectoderm and also

57 have baseline apical myosin levels, maintain an almost constant apical area throughout the
58 folding process (Rauzi et al., 2015). We investigated how this tissue-wide pattern of cell shapes
59 is established and how it impacts the resulting tissue shape.

60 Mesoderm cell shape change and cell fate are initially driven by the transcription factors
61 Dorsal, Twist, and Snail (Boulay et al., 1987; Furlong et al., 2001; Leptin, 1991; Thisse et al.,
62 1988), which exhibit distinct expression patterns. Nuclear Dorsal is present in a ventral-dorsal
63 gradient that narrows over time (Rahimi et al., 2019; Roth et al., 1989; Rushlow et al., 1989;
64 Steward, 1989; Steward et al., 1988). Measurements of the transcription dynamics of Twist
65 target genes, *T48* and *fog*, demonstrate that downstream Twist targets are expressed first at the
66 ventral midline and subsequently expand laterally (Lim et al., 2017). This temporal progression
67 of gene expression results in the graded accumulation of T48 transcripts and protein along the
68 ventral-lateral axis (Heer et al., 2017; Lim et al., 2017; Rahimi et al., 2019). Snail can both
69 activate and repress gene expression (Rembold et al., 2014). One gene that is activated by
70 Snail is the G-protein coupled receptor (GPCR) Mist (Manning et al., 2013). In contrast to
71 graded Twist activity, Snail activity as assessed by Mist mRNA expression is uniform across the
72 mesoderm (Lim et al., 2017). Therefore, Twist and Snail target genes appear to have distinct
73 patterns of expression.

74 The product of the Twist target gene *fog* activates the Mist GPCR and a uniformly
75 expressed GPCR, Smog (Costa et al., 1994; Kerridge et al., 2016; Manning et al., 2013). This
76 GPCR pathway and T48 expression act via the guanine nucleotide exchange factor (GEF)
77 RhoGEF2 and the small GTPase RhoA to activate myosin contractility (Barrett et al., 1997;
78 Hacker and Perrimon, 1998; Kolsch et al., 2007). Functioning in opposition to RhoGEF2 to shut
79 off RhoA signaling activity is the RhoA GTPase-activating protein (GAP) C-GAP (also called
80 Cumberland-GAP or RhoGAP71E) (Mason et al., 2016). RhoA coordinately activates myosin,
81 via Rho-associated and coiled coil kinase (ROCK), and actin filament (F-actin) assembly, via the
82 formin Diaphanous (Dawes-Hoang et al., 2005; Homem and Peifer, 2008). Myosin activation

occurs in a gradient that is narrower than the gradient of T48 protein accumulation (Heer et al., 2017), but it is not known whether RhoA activation follows a similar pattern to T48 or whether RhoA signaling is refined by its regulators. F-actin is apically enriched in ventral cells in a manner that depends on RhoA signaling (Fox and Peifer, 2007). We asked whether there is a multicellular pattern to F-actin across the mesoderm and how this is controlled transcriptionally and via RhoA signaling.

Here we show a tissue-level pattern of junctional F-actin density that is distinct from myosin activation and Twist activity. This pattern of junctional F-actin results from the combination of Snail-dependent depletion and Twist-dependent accumulation, which is tuned by RhoA activity level. We show that the width of the actomyosin gradient regulates tissue curvature, as well as lumen size in the mesodermal tube structure generated by this fold. Our results show how combinatorial patterning of two transcriptional programs creates distinct zones of cytoskeletal protein accumulation across the mesoderm and that this patterning promotes proper tissue curvature.

Results

Junctional F-actin exhibits a distinct tissue pattern from apical myosin during mesoderm invagination

To determine how the ventral-dorsal pattern of F-actin changes during mesoderm invagination, we labeled F-actin in fixed or live embryos with phalloidin or Utrophin::GFP, respectively, and measured F-actin in cell bins at defined positions from the ventral midline. We chose to focus our analysis on junctional F-actin density, because cortical F-actin density is known to affect cell mechanics (Salbreux et al., 2012; Stricker et al., 2010) and we observed clear variation of junctional F-actin across the mesoderm and neighboring ectoderm. Before ventral furrow formation onset, mesodermal junctional F-actin density (and integrated F-actin intensity) drops relative to ectoderm cells (Fig. 1 B and D and Supplemental Fig. 1 A - C), consistent with what has been previously observed (Jodoin et al., 2015).

During ventral furrow formation, junctional F-actin density rose around the ventral midline and exhibited a gradient that extended to cell 6, similar to apical myosin (Fig. 1 C, D, and Supplemental Fig. 1 A - C). F-actin density remained lower in cell rows ~ 6 - 8 of the mesoderm, forming a zone of junctional F-actin depletion relative to the neighboring ectoderm. This contrasts with apical myosin activation, which decreases to a baseline level in marginal mesoderm cells that is similar to the neighboring ectoderm (Fig. 1 A) (Heer et al., 2017; Lim et al., 2017; Spahn and Reuter, 2013). The observed pattern was also present in live embryos expressing the actin-binding domain of Utrophin fused to green fluorescent protein (Utrophin::GFP) or mCherry (Utrophin::mCherry), but not with a general membrane marker, Gap43-mCherry, indicating that this measurement is not a fixation artifact or due to changes in plasma membrane structure, such as stretching (Supplemental Fig. 1 D). Thus, junctional F-actin levels exhibit a distinct pattern from that of apical myosin activation.

123 The observed tissue-wide pattern of F-actin density matched the pattern of apical cell
124 area constriction and stretching (Fig. 1 A, C; Supplemental Fig. 1A). To quantify the strength of
125 this relationship, we correlated junctional cell F-actin density with apical cell area in both
126 mesoderm and adjacent ectoderm cells (Fig. 1 E). We found an anti-correlation between
127 junctional F-actin density and apical area (R-squared: 0.1083), in part, because marginal
128 mesoderm cells (green/yellow points) had low F-actin and were stretched and adjacent
129 ectoderm cells (red) had intermediate F-actin and did not stretch or constrict. Because F-actin
130 density and turnover influence the ability to dissipate stress (Clement et al., 2017; Salbreux et
131 al., 2012; Stricker et al., 2010), our result suggests that lower F-actin levels allow lateral
132 mesoderm cells to stretch, resulting in an inverted cell morphology for cells at the edge of the
133 mesoderm compared to apically constricted cells at the ventral midline.

134

135 **Snail and Twist regulate distinct components of the F-actin pattern**

136 To determine how this tissue-wide F-actin pattern is established, we tested how the transcription
137 factors *snail* and *twist* affect junctional F-actin density. Snail activity in the mesoderm, as
138 measured by *mist* transcription, is uniform (Lim et al., 2017) and we found that the Snail
139 boundary co-localizes precisely with the F-actin depletion boundary (Fig. 2 A). Furthermore,
140 mesodermal cell junctional F-actin depletion requires *snail*. To illustrate and quantify junctional
141 F-actin around the curved embryo, we created a reslice at a constant height from the apical
142 surface (Supplemental Fig. 2). Unlike control (heterozygous) embryos, *snail* homozygous
143 mutant embryos expressing fluorescently tagged Utrophin do not exhibit patterned junctional F-
144 actin levels in the ventral region, but rather uniform intensity throughout the region, without a
145 sharp boundary (Fig. 2 B and C). Because *snail* mutant embryos were imaged live, we could
146 identify the mesoderm/ectoderm boundary based on subsequent germband extension

147 movements in the ectoderm and premature cell divisions that occurred in the uninternalized
148 mesoderm, which is mitotic domain 10 (Foe, 1989; Grosshans and Wieschaus, 2000). We
149 conclude that Snail decreases junctional F-actin density in the mesoderm.

150 In contrast to Snail, the expression of Twist transcriptional targets is graded, with Twist
151 target expression initiating first along the ventral midline and then expanding laterally (Lim et al.,
152 2017; Rahimi et al., 2019). Twist also regulates *snail* expression; *twist* mutants reduce *snail*
153 expression width (Leptin, 1991). To determine *twist*'s requirement for the tissue-wide pattern of
154 junctional F-actin, we examined F-actin density in a *twist* null mutant that has been shown to
155 disrupt myosin stabilization, but still exhibits transient actomyosin contractions (Martin et al.,
156 2009). In contrast to *snail* mutants, *twist* mutant embryos exhibit lower junctional F-actin density
157 in the mesoderm and a clear boundary with the ectoderm (Fig. 2 D, E, and F). However, the
158 zone of low junctional F-actin is decreased to half the normal width, consistent with narrowed
159 *snail* expression depleting F-actin in a narrower mesoderm. Graded F-actin accumulation
160 around the ventral midline was absent in *twist* mutants, suggesting that higher F-actin density at
161 the midline depends on the Twist pathway, which includes RhoA activation (Dawes-Hoang et
162 al., 2005; Fox and Peifer, 2007; Kolsch et al., 2007; Mason et al., 2013). Therefore, mesodermal
163 control of junctional F-actin by Twist and Snail is comprised of two nested layers: 1) prior to
164 ventral furrow formation, uniform Snail activity lowers F-actin density across the mesoderm, and
165 2) during ventral furrow formation there is a Twist-dependent increase in F-actin density that,
166 similarly to apical myosin, creates a ventral-lateral gradient, but also creates a 'valley' in
167 junctional F-actin density at the margin of the mesoderm.

168

169 **Neither graded myosin activation nor F-actin depletion depend on intercellular**
170 **mechanical connections or cell shape change**

171 Our data suggested that Snail and Twist promote uniform mesodermal F-actin depletion prior to
172 apical constriction and subsequent graded actomyosin accumulation, respectively. In the ventral
173 furrow and the related process of *Drosophila* posterior midgut formation, it has been proposed
174 that mechanical feedback between constricting cells is required to induce myosin accumulation,
175 which may contribute to a gradient or wave in contractility (Bailles et al., 2019; Mitrossilis et al.,
176 2017). Therefore, it was important to determine whether transcriptional activity is directly
177 shaping these patterns or whether mechanical induction of myosin contributes as well.

178 To determine the contribution of intercellular mechanical connections to the multicellular
179 patterns of myosin activation and junctional F-actin density, we examined embryos in which
180 intercellular cytoskeletal coupling was disrupted. We did this by depleting the adherens junction
181 protein α-catenin by RNA interference (α-catenin-RNAi), which uncouples the cytoskeletal
182 meshwork of cells from the junctions and, thus, mechanical connections between cells (Fig. 3 A,
183 Supplemental Movie S1, 2) (Fernandez-Gonzalez and Zallen, 2011; Martin et al., 2010; Yevick
184 et al., 2019). In α-catenin-RNAi embryos, ventral cell apical area remains at pre-gastrulation
185 levels (about 40 μm^2), but myosin contracts into spot-like structures (Fig. 3 A, B, E) (Martin et
186 al., 2010). Apical myosin quantification showed that, despite the lack of mechanical coupling,
187 myosin reproducibly accumulates in a gradient around the ventral midline that is similar to the
188 wild-type gradient (Fig. 3 C, E). Therefore, graded myosin activation across the tissue does not
189 depend on force transmission between cells.

190 Adherens junctions are a known target of Snail in the mesoderm (Chanet and
191 Schweisguth, 2012; Dawes-Hoang et al., 2005; Kolsch et al., 2007) and E-cadherin exhibits a
192 similar tissue-level pattern to F-actin (Supplemental Fig. 3A). Therefore, we asked whether
193 mesodermal F-actin depletion depended on intact adherens junctions. Similar to wild-type
194 embryos, junctional F-actin density in α-catenin-RNAi embryos is low across the mesoderm with
195 a sharp boundary to the ectoderm (Fig. 3 D, E). This observation suggests that the Snail-

196 mediated F-actin density reduction does not depend on intact junctions. Furthermore, low F-
197 actin density in lateral mesoderm cells is maintained despite a lack of apical constriction and
198 stretching of lateral mesoderm cells, confirming that reduced F-actin density in these cells is not
199 due to cell stretching. Interestingly, junctional F-actin levels around the midline does not appear
200 to increase the same in α-catenin-RNAi embryos as in wild-type embryos during constriction.
201 The lack of increased F-actin density may be due to disrupted intercellular junctions in the α-
202 catenin-RNAi embryos, but it is also possible that the increased junctional F-actin density at the
203 midline in wild-type/control embryos is due to apical constriction. Medio-apical F-actin foci,
204 which co-localize with myosin, appear in α-catenin-RNAi embryos, and it is possible that
205 elevated junctional F-actin is drawn in to these structures (Supplemental Fig. 3 B). These results
206 indicate that F-actin depletion in the mesoderm does not require intact adherens junctions or
207 mechanical coupling of cells, which is consistent with transcriptional regulation causing the
208 observed pattern.

209

210 **RhoA activation occurs in a gradient**

211 We next investigated further what is responsible for the gradient in apical myosin and junctional
212 F-actin. Fog and T48 transcripts accumulate in a gradient (Lim et al., 2017; Rahimi et al., 2019),
213 but the width of T48 protein accumulation is wider than the gradient in apical myosin (Heer et
214 al., 2017). Because Fog and T48 function upstream of RhoA, we examined fluorescently tagged
215 versions of RhoA's activator RhoGEF2 (under an endogenous promoter), the Anillin Rho-
216 binding domain (an active RhoA sensor), and the RhoA effector ROCK (Mason et al., 2016;
217 Munjal et al., 2015; Simoes Sde et al., 2010) (Fig. 4 A). Each of these fluorescent protein
218 markers became apically enriched in ventral cells during ventral furrow formation, consistent
219 with previous studies (Fig. 4 B) (Kolsch et al., 2007; Mason et al., 2013; Mason et al., 2016).

220 Quantification of apical fluorescence by cell row revealed that all three markers for RhoA
221 pathway activation were graded along the ventral-lateral axis, exhibiting strong fluorescence at
222 the ventral midline and gradually decreasing to baseline after ~ 6 cells (Fig. 4 B and C). In
223 contrast, endogenously tagged C-GAP-GFP was largely cytoplasmic and appeared uniform
224 across the ventral domain during folding (Supplemental Fig. 4 A). Therefore, there is a ventral-
225 lateral gradient of RhoA activation in the mesoderm. We next tested how the RhoA gradient
226 affects graded apical myosin and junctional F-actin.

227

228 **RhoGEF and GAP modulate actomyosin gradient width**

229 The gradient in accumulated T48 transcripts and protein extends beyond the 5-6 cell rows from
230 the ventral midline where we detect RhoA and myosin activation (Heer et al., 2017; Lim et al.,
231 2017; Rahimi et al., 2019). Therefore, we hypothesized that the signaling network downstream
232 of T48 further shapes the contractile gradient. Mesodermal RhoA signaling involves a signaling
233 circuit, which includes an activator/inhibitor pair (Fig. 4 A). The activator RhoGEF2 is required
234 for high levels of apical myosin accumulation (Dawes-Hoang et al., 2005; Nikolaidou and
235 Barrett, 2004). Severely depleting the inhibitor, C-GAP, disrupts proper subcellular myosin
236 localization (Mason et al., 2016). To test the importance of this circuit in regulating the
237 multicellular patterning of the actin cytoskeleton, we either depleted or overexpressed the RhoA
238 regulators C-GAP or RhoGEF2, and determined the effect on actomyosin distribution.

239 First, we examined apical myosin after elevating RhoA activation by either depleting C-
240 GAP by RNAi (C-GAP-RNAi) or overexpressing RhoGEF2 (RhoGEF2 O/E). These
241 perturbations elevate myosin in mesoderm cells, whereas there is still no noticeable myosin
242 accumulation in the ectoderm at this stage (Fig. 5 A, B). C-GAP-RNAi and RhoGEF2 O/E
243 expand the myosin gradient width, with myosin activation occurring 1 – 2 cell rows farther from

244 the ventral midline than control embryos (Fig. 5 C, D). C-GAP-RNAi also expands the zone of
245 upstream RhoA activation and downstream apical constriction around the ventral midline (Fig. 5
246 C and Supplemental Fig. 5 A). Similar to C-GAP-RNAi, RhoGEF2 O/E expands the zone of
247 apical constriction, although cells at the ventral midline constrict less than in control embryos
248 (Fig. 5 D). Interestingly, decreasing RhoA activation by RhoGEF2 depletion (RhoGEF2-RNAi)
249 does not narrow the myosin gradient, although the overall levels and uniformity of cellular
250 myosin (and constriction) are decreased (Supplemental Fig. 5 B). Overall, our data show that
251 increasing RhoA activity increases the width of the myosin gradient, with C-GAP playing an
252 integral role in restricting myosin gradient width.

253 To determine whether RhoA activation is critical for regulation of the junctional F-actin
254 pattern, we examined junctional F-actin density after either elevating or depleting RhoA activity.
255 Elevating RhoA activation, either by C-GAP-RNAi or RhoGEF2 O/E increases junctional F-actin
256 density in marginal mesoderm cells, causing them to be more similar to ectoderm cells (Fig. 5
257 E-H). In some cases, RhoGEF2 O/E completely eliminates the pattern of F-actin depletion and
258 elevation across the mesoderm (Fig. 5 G, H). Conversely, decreasing RhoA activity by
259 RhoGEF2-RNAi further depletes junctional F-actin in marginal mesoderm cells (Fig. 5 F).
260 Overall, our data suggest that RhoA activity regulates myosin gradient width and also the
261 pattern of junctional F-actin density across the mesoderm.

262

263 **Myosin pulses elicit different area responses in midline versus marginal mesoderm cells**

264 Myosin pulses are discrete events in which there is a burst of myosin accumulation and
265 constriction of the cell apex. RhoA activity levels determine the contractile outcome of a myosin
266 pulse in individual cells during ventral furrow formation (Mason et al., 2016). Given that RhoA
267 activity is graded across the furrow (Fig. 4), we examined the behavior of myosin pulses

268 throughout the mesoderm. There are distinct classes of myosin pulses that occur during furrow
269 formation. 'Ratcheted pulses' are events in which apical, active myosin persists after a pulse
270 and decreased apical area is sustained (Fig. 6 A) (Xie and Martin, 2015). In contrast,
271 'unratcheted pulses' exhibit myosin dissipation after the pulse and cell relaxation follows
272 constriction. There is a continuum of behaviors from ratcheted to unratcheted, which are
273 associated with high and low RhoA activity, respectively (Mason et al 2016).

274 To determine whether the ventral-lateral gradient in RhoA patterns myosin pulse type,
275 we examined myosin persistence across different cell rows. Consistently with previous
276 measurements of contractile pulses in the middle of the ventral furrow (Xie and Martin, 2015),
277 pulses close to the ventral midline exhibit persistent myosin; the myosin level after the pulse is
278 higher than the initial baseline (Fig. 6 B, cell row 1). Myosin persistence is associated with a
279 sustained decrease in apical area (Fig. 6 C, cell row 1) (Xie and Martin, 2015). In contrast,
280 myosin pulses at the margin of the mesoderm do not exhibit strong myosin persistence (Fig. 6
281 B, cell row 7). These myosin pulses accompany cell stretching and do not robustly result in cell
282 apex constriction (Fig. 6 C, cell row 7). Comparing pulse behavior across different ventral-lateral
283 positions, we find a graded decrease in myosin persistence and area stabilization after pulses
284 with distance from the ventral midline (Fig. 6 D).

285 To further differentiate myosin pulse behaviors, we compared the cross-correlation
286 between the constriction rate and the rate of myosin change in cells along the ventral-lateral
287 axis. Cells closest to the ventral midline exhibit the strongest positive correlation, indicating a
288 correspondence between myosin increase and constriction (Fig. 6 E). Peak correlation is
289 highest in cells along the ventral midline and decreases gradually as distance from the ventral
290 midline increases (Fig. 6 E). Cells ~7-8 rows from the midline exhibit a small negative
291 correlation, indicating that these cells are prone to not constricting, or may even increase their
292 area during myosin pulses (Fig. 6 F). This behavior is specific to mesoderm cells at this stage

293 because ectoderm cells do not exhibit either a clear positive or negative correlation (Fig. 6 G,
294 cell rows 11, 12). This suggests that the RhoA gradient creates a gradient in cell behaviors
295 coincident with myosin pulses, which we speculate contributes to the transition from constricting
296 to stretching with distance from the midline.

297

298 **Actomyosin gradient width regulates furrow curvature and lumen size**

299 To examine the role of the wild-type contractile pattern in successful ventral furrow formation,
300 we tested how disrupting this pattern affects tissue shape. In wild-type embryos with graded
301 constriction, the ventral furrow is a sharp, v-shaped fold with high curvature at its center (Fig.
302 7A). Previous work showed that globally changing cell fate by altering the *dorsal* gradient to
303 expand the mesoderm results in a flattened depression (Heer et al., 2017). Here, we
304 investigated the role of the actomyosin gradient in tissue folding, by directly modulating RhoA
305 activity without changing mesoderm width. Upon identifying C-GAP, we found that some C-
306 GAP-RNAi embryos have a more C-shaped, less sharp fold (Mason et al., 2016). However, the
307 cause of this abnormal shape was not clear. Therefore, we tested whether widening the
308 gradient by C-GAP-RNAi or RhoGEF2 O/E affects ventral furrow curvature. C-GAP-RNAi
309 embryos in which the zone of uniform constriction is wider have lower central curvature than in
310 wild type (Fig. 7 A and C, Supplemental Fig. 7 A and B). RhoGEF2 O/E embryos also have
311 lower central curvature, suggesting that increased actomyosin gradient width decreases tissue
312 curvature (Fig. 7 B and C, Supplemental Fig. 6 A and B). Indeed, we found that there is an
313 anticorrelation between gradient width and tissue curvature across embryos of different
314 genotypes (Fig. 7 E). Most embryos still fold successfully, although some extreme cases do not
315 manage to internalize the mesoderm. Successful folding in C-GAP-RNAi and RhoGEF2 O/E

316 embryos is associated with a significantly enlarged lumen when invaginated mesoderm forms a
317 tube (Fig. 7D).

318 To further determine the relationship between junctional F-actin density and curvature,
319 we also decreased RhoA activation. Decreasing RhoA activation by RhoGEF2-RNAi in
320 Utrophin::GFP expressing embryos enabled us to observe the effect of lower F-actin levels in
321 marginal mesoderm cells on folding (Fig. 5 F). These embryos have increased central curvature
322 compared to control embryos (Supplemental Fig. 6 A, B). Although RhoGEF2-RNAi embryos
323 fold successfully, some subsequently exhibit divisions at the embryo surface, suggesting that
324 the mesoderm, which comprises mitotic domain 10, is not completely internalized
325 (Supplemental Movie S3, 4). Overall, our data suggest that the multicellular gradient shape and
326 the F-actin levels in marginal mesoderm cells influence tissue curvature during ventral furrow
327 formation.

328

329

330 **Discussion**

331 Here, we discovered a distinct pattern of junctional F-actin across the *Drosophila* mesoderm
332 and showed how it emerges from the combination of overlapping patterns of transcriptional
333 activity (Fig. 7 F). We showed that Snail-dependent uniform depletion of junctional F-actin
334 throughout the mesoderm, plus Twist-dependent junctional F-actin accumulation in a gradient
335 around the ventral midline, pattern F-actin across the ventral side of the embryo. In addition, we
336 showed that RhoA regulation by the balance of RhoGEF2 to C-GAP determines the actomyosin
337 gradient width. Importantly, the levels and dynamics of F-actin and myosin in distinct cell groups
338 are correlated with their shape changes, leading us to speculate that differences in F-actin
339 density, turnover, and/or myosin persistence between cell groups determine apical constriction
340 vs. stretching behavior across the ventral domain.

341 **Combination of Twist and Snail creates distinct zones of junctional F-actin density**

342 Prior to folding, we observed through live imaging that Snail expression results in uniform
343 junctional F-actin depletion of mesoderm cells. During folding, Twist expression results in a
344 gradient of junctional F-actin accumulation in a manner that depends on RhoA signaling and
345 adherens junctions. Cells with high F-actin levels tend to maintain their shape or constrict,
346 whereas low-F-actin cells stretch. It was possible that cell strain/stretching or constriction
347 contributed to differences in F-actin density (Latorre et al., 2018). However, the fact that F-actin
348 depletion preludes stretching and is not disrupted when cells are prevented from constricting
349 and stretching their neighbors suggests that F-actin depletion is not a consequence of cell
350 shape. The role of F-actin cortex density in a cell's response to mechanical stress is well
351 documented (Stricker et al., 2010). In the marginal mesoderm, lower F-actin density in
352 stretching cells is compounded by lower levels of zonula adherens proteins (Dawes-Hoang et
353 al., 2005; Kolsch et al., 2007; Weng and Wieschaus, 2016), both of which could promote the

354 ability of these cells to remodel and stretch in response to stress. In contrast, the neighboring
355 ectoderm and the medial ventral cells have high F-actin and adherens junction density, which
356 may help those cells maintain their shape under stress (Rauzi et al., 2015).

357 **RhoA activity level determines the width of the actomyosin gradient**

358 Nested within this zone of Snail-mediated F-actin depletion, Twist activity causes
359 actomyosin accumulation via graded RhoA activation. The combination of these overlapping
360 transcriptional patterns allows for domains of different cell behaviors and mechanical properties
361 within a tissue of uniform cell fate (the mesoderm). RhoGTPases are regulated by complex
362 interactions between their (activating) GEFs and (inhibiting) GAPs in many contexts (Denk-
363 Lobnig and Martin, 2019). In the ventral furrow specifically, interactions between C-GAP and
364 RhoGEF2 tune sub-cellular localization and dynamics of the contractile apparatus during folding
365 (Mason et al., 2016). Here, we found that changes to C-GAP or RhoGEF2 levels, at a dose that
366 does not strongly disrupt cell-level organization, change the multicellular pattern of actomyosin
367 levels across the ventral domain. For example, C-GAP-RNAi and RhoGEF2 O/E both widen the
368 myosin gradient and elevate junctional F-actin levels in the marginal mesoderm. Conversely,
369 RhoGEF2-RNAi causes reduced F-actin density in marginal mesoderm cells.

370 These specific pattern changes can be explained by a model in which there is a graded
371 activator (RhoGEF2) and a uniform inhibitor (C-GAP). In this case, the inhibitor can buffer
372 activation and create a threshold for activation, which would regulate the width of the
373 actomyosin gradient. A prediction of this model is that the gradient widens if overall activator
374 levels increase or inhibitor levels decrease. Furthermore, the upstream activator (RhoGEF2)
375 should be graded over a wider region in wild-type than the downstream myosin. Our
376 measurements of RhoGEF2::GFP show a gradient more similar to the width of apical myosin
377 than upstream pathway components, such as T48 protein (Heer et al., 2017). This could be due

378 to the small signal-to-noise ratio of the RhoGEF2::GFP probe, or due to possible feedback in
379 the RhoA pathway (Priya et al., 2015). In contrast to RhoGEF2 overexpression, RhoGEF2
380 depletion does not change the myosin gradient width, but results in lower F-actin levels in the
381 marginal mesoderm cells, which could reflect a narrower gradient of F-actin.

382 Our data show that the gradient shape is tuned by activator-inhibitor balance at the level
383 of direct RhoA regulation. There are other points in the pathway where balance between
384 inhibition and activation is important and could contribute to tissue-wide patterning. In particular,
385 GPRK2, an inhibitor of GPCR signaling, affects myosin organization and cell behaviors (Fuse et
386 al., 2013; Jha et al., 2018). In GPRK2 mutant embryos, apical constriction is expanded, such
387 that lateral mesoderm cells that normally stretch accumulate myosin and constrict (Fuse et al.,
388 2013). This is consistent with a potential role for GPRK2 restricting the contractile gradient.
389 Further downstream, myosin activity is directly regulated by the balance of ROCK and myosin
390 phosphatase (Munjal et al., 2015; Vasquez et al., 2014). Regulation of tissue-wide properties by
391 overlapping patterns of activator and inhibitors, such as F-actin regulation by Snail and Twist
392 and actomyosin gradient regulation by C-GAP and RhoGEF2, is an intriguing method to create
393 complex spatial patterns of mechanical cell behavior and morphogenesis.

394 **Fold curvature is tuned by tissue-wide actomyosin patterning**

395 Our disruptions of the actomyosin gradient and the resulting changes in tissue shape suggest
396 that the tissue-wide pattern of the actin cytoskeleton regulates shape. We showed that changing
397 the actomyosin gradient width by modulating the levels of RhoGEF2 or C-GAP effects a change
398 in tissue curvature. Elevating RhoA activity creates a wider gradient and results in C-shaped
399 furrows with low curvature. We showed that the width of the myosin gradient for an individual
400 embryo during flattening is predictive of its furrow and post-fold shape. This is consistent with
401 theoretical work that suggested a broadening contractility would lower tissue curvature (Heer et

402 al., 2017). Another supporting example is that in GPRK2 mutants, all cells within the mesoderm
403 (~18 cells) constrict and create a U-shaped furrow that often fails to close (Fuse et al., 2013).

404 That increased contractility in the tissue decreases fold curvature may seem counter-
405 intuitive, but one has to consider the force balance between contractile cells in the tissue. For
406 example, expanding the domain of contractile cells prevents efficient apical constriction at the
407 ventral midline (Chanet et al., 2017; Heer et al., 2017), which we also observed for RhoGEF2
408 O/E embryos. In many other cases, it has been shown that the successful constriction and
409 invagination of cells depends on neighboring tissue mechanics (Ko et al., 2020; Perez-Mockus
410 et al., 2017; Sui et al., 2018). RhoGEF2-RNAi embryos do not alter the width of the myosin
411 gradient, but have lower junctional F-actin density in marginal mesoderm cells. RhoGEF2
412 embryos with lower F-actin in the marginal mesoderm have higher furrow curvature. Therefore,
413 it is plausible that the stretching marginal mesoderm cells can promote efficient apical
414 constriction and the creation of a sharp fold at the ventral midline. Together with these past
415 studies, our work emphasizes the importance of understanding tissue-wide patterns in
416 cytoskeletal proteins during folding.

417 Development generates a multitude of different curvatures and shapes for different
418 contexts. We showed that tissue curvature is sensitive to changes in the pattern of actomyosin
419 within the mesoderm, suggesting that gene expression patterning is an effective way to tune
420 curvature. Given the importance of this patterning mechanism in regulating tissue shape, it is
421 likely that mechanical cell properties are patterned and tuned across the tissue similarly in other
422 developmental contexts with different curvature requirements.

423

424 **Materials and Methods**

425 **Fly stocks and crosses**

426 See Supplemental Table S1.

427 A C-terminal GFP tag was inserted at the endogenous C-GAP locus using CRISPR-
428 Cas9 as previously described (Gratz et al., 2015). Coding sequences for two 15 base pair (bp)
429 gRNAs targeting neighboring sites 5' of the *rhoGAP71E* gene start codon were cloned into the
430 pU6-BbsI plasmid using the CRISPR Optimal Target Finder (Gratz et al., 2014; Iseli et al.,
431 2007). The donor template plasmid for homology directed repair was generated using
432 Exponential Megapriming PCR (Ulrich et al., 2012). A plasmid backbone (from pHD scarless DS
433 Red) containing an ampicillin resistance gene and an origin of replication was combined with
434 two homology arms (1219 bp and 1119bp, respectively) homologous to the region around the
435 *rhoGAP71E* gene start codon, flanking a *GFP* encoding DNA sequence (kindly provided by Iain
436 Cheeseman) with a N-terminal 4 amino acid-encoding linker region (Ser-Gly-Gly-Ser). Both
437 plasmids were injected into nanos>Cas9 expressing embryos. Surviving adults were crossed to
438 y, w; +; + flies and then screened for mosaic GFP insertion by PCR. Progeny of GFP-positive
439 injected flies were crossed to y, w; +; Dr/TM3 flies and then screened by PCR for the GFP
440 insertion. Successful insertions were further analyzed by sequencing. The fly stock established
441 from their offspring was later back-crossed once to OreR flies in order to eliminate potential off-
442 target mutations.

443 **Live and fixed imaging**

444 Embryos were collected in plastic cups covered with apple-juice plates. Flies were
445 allowed to lay eggs for 2–4 h at 18-25 °C. The plate was removed and the embryos immersed in
446 Halocarbon 27 oil for staging. Cellular blastoderm stage embryos were collected and prepared

447 for imaging. Embryos were dechorionated with 50% bleach, rinsed with water, and then
448 mounted on a slide with embryo glue (Scotch tape resuspended in heptane), with the ventral
449 side facing upwards. A chamber was made with two no. 1.5 coverslips as spacers, a no. 1.0
450 coverslip placed on top, and the chamber was filled with Halocarbon 27 oil before imaging.
451 Images were acquired on a Zeiss 710 microscope with an Apochromat 40×/1.2 numerical
452 aperture W Korr M27 objective.
453 Immuno- and phalloidin staining was performed using standard methods (Martin et al.,
454 2009). Embryos were fixed with 4% paraformaldehyde/heptane for 30 min, devitellinized
455 manually, stained with phalloidin, primary antibodies and appropriate fluorescently tagged
456 secondary antibodies, and mounted in AquaPolymount (Polysciences, Inc.). Anti-snail (rabbit,
457 1:100, M. Biggin, Lawrence Berkeley National Lab), anti-GFP (rabbit, 1:500; Abcam, ab290) and
458 anti-E-cadherin (rat, 1:50; DHSB) antibodies and AlexaFluor568 phalloidin (Invitrogen) were
459 used. All imaging was carried out on a Zeiss 710 confocal microscope with a Plan-Apochromat
460 40×/1.2 numerical aperture W Korr M27 objective.
461 For imaging settings, refer to Supplemental Table S2.

462

463 **Gradient analysis**

464 Analysis was done as described in Heer et al. 2017. All image analysis was performed in
465 Fiji (http://fiji.sc) (Schindelin et al., 2012) and MATLAB (MathWorks). Custom software for
466 image processing is available upon request.

467 *Definition of developmental timing*

468 Wild-type embryos were staged based on the time of folding. The accuracy of this
469 method was confirmed by comparing constricted areas per bin at the selected time point. For

470 embryos with disrupted constriction and folding, an analogous time point was chosen relative to
471 the beginning of myosin/ fluorescence accumulation.

472 *Shell projection and thresholding to measure apical fluorescence intensity*

473 Shell projections of the apical surface were made to capture the embryo surface. First,
474 cytoplasmic background signal (defined as the mean cytoplasmic signal plus 2.5 standard
475 deviations) was subtracted from the myosin channel (Martin et al., 2009; Vasquez et al., 2014).
476 For non-myosin fluorescent signal (Fig. 3), the cytoplasmic background subtraction was
477 adjusted to account for differences in signal-to-noise ratio for different fluorescent markers
478 (RhoGEF2-GFP: mean + 2 standard deviations (SDs); aniRBD-GFP: 2 SDs, rok-GFP: 2.5 to 3
479 SDs).

480 The maximum myosin (or other apically enriched fluorescent) signal intensity in the *z*-
481 plane was used to generate a rough map of the embryo surface. A Fourier transform was used
482 to generate a smooth continuous surface. Myosin signal was averaged over the 4 μm above the
483 surface of detected maximum intensity and membrane signal was the sum of the signal from 1
484 μm below the surface. A gaussian blur filter (radius 1 pixel for fluorescent signal, 0.7-1
485 membranes) was applied after shell projection to reduce noise.

486 Shell projections from live and immunostained images were then segmented using an
487 existing MATLAB package, Embryo Development Geometry Explorer (EDGE) (Gelbart et al.,
488 2012). Membrane signal (Gap43::mCherry) or cortical actin (phalloidin) projections were used to
489 detect cell boundaries (and track cells in time for live images). Errors in segmentation were
490 corrected manually. Our segmentation algorithm was used to determine centroid position, cell
491 diameter, cell area, cell perimeter of segmented cells as well as total myosin/fluorescent signal
492 per cell based on the corresponding myosin/fluorescent channel projection.

493 *Defining cell bins*

494 For all image quantifications, data was aggregated into ‘cell bins’ (Heer et al., 2017) .
495 Cells were assigned to bins based on the ventral-lateral position of the cell centroid relative to
496 the ventral midline. The ventral midline (VM) was defined as the position at which the furrow
497 closes. In fixed images or for embryos that did not fold (or rotated while folding), the position of
498 the VM was determined by symmetry of the fluorescent signal. Live images with several
499 segmented time points were binned based on initial position of the cell centroid before
500 constriction and folding; the boundaries of the bins were set based on the average cell diameter
501 along the ventral-lateral axis. For images in which cells had already started to constrict, the
502 width of each bin was set manually (but still relative to average cell diameter) to approximate the
503 width of cells at that ventral-lateral position. We used MATLAB to generate box-and-whiskers
504 plots depicting the distribution of data, overlaid with the mean of each bin. For boxplots, bottom
505 and top sides of the box represent 25th and 75th percentile of cells, respectively. Outliers were
506 defined as values 1.5 times bigger than the interquartile range. Fluorescent signal was
507 normalized by dividing by the mean of the bin with highest average intensity, to adjust for
508 variability in imaging conditions.

509 *Junctional F-actin quantification*

510 For apical projections of phalloidin staining (Fig.1 A, 2 A and 4 B), embryos were shell-
511 projected and cells tracked similarly to myosin and other markers (see above), but no
512 background subtraction was required because of the low background staining for phalloidin
513 stained embryos. For analysis, junctional signal was extracted from the apical shell projection by
514 only using signal within 2 μm of the tracked cell boundaries. This total junctional F-actin signal
515 was divided by the cell perimeter to obtain junctional F-actin density independently of cell
516 circumference.

517 Because mesodermal F-actin depletion was most obvious subapically, not apically, with
518 fluorescently tagged Utrophin markers in live embryos (Fig. 2 B, 5 C and 7 C), those movies
519 were “shell-projected” in Fiji by generating a Z-reslice (1 μm per slice) and then doing a second
520 reslice along a manually drawn, subapical segmented line that followed the ventral-lateral
521 curvature of the embryo surface (Supplemental Fig. 2). This allowed us to account for specific
522 ventral-lateral curvature and get a subapical projection at a consistent apical-basal depth. The
523 center part along the AP axis of the shell-projection, where anterior-posterior (AP) curvature is
524 small, was used to quantify F-actin (Utrophin::mCherry or ::GFP) intensity along the ventral-
525 lateral axis. For analysis of the tissue-wide pattern, junctional signal was extracted from the
526 subapical shell projection by only using signal within 2 μm of the tracked cell boundaries. This
527 total junctional F-actin signal was divided by the cell perimeter to obtain junctional F-actin
528 density independently of cell size.

529

530 **Pulsing analysis**

531 Images of live embryos with myosin and membrane markers during folding were
532 obtained as above, but with faster scan speed and smaller z-depth, to obtain time steps
533 between 6 and 10 seconds, which is sufficient to capture typical myosin and area pulsing
534 behavior (Martin et al 2009). Cells across the mesoderm were tracked over time using EDGE
535 and cell area and myosin intensity were exported. In Matlab 2019a, we detected peaks within
536 individual cells of maximal myosin intensity increase by smoothing with a moving average filter
537 and then detecting local maxima. The myosin intensity and cell area behavior about 100
538 seconds before and after each maximum was saved as a trace. Pulse traces were averaged for
539 each cell bin to identify average behavior based on ventral-lateral cell position. Myosin
540 persistence was defined as the minimum myosin intensity within each trace after a myosin pulse

541 minus the minimum myosin intensity before the same pulse. Persistence of area constriction
542 was defined as the maximum cell area after a myosin pulse minus maximum cell area before
543 the same pulse. Persistence values were averaged by bin and plotted in Matlab for three
544 individual embryos.

545 To analyze how the relationship between area and myosin behaviors changes based on
546 cell position, we cross-correlated myosin and area behavior (as described in Martin et al. 2009).
547 We used the xcorr function in Matlab to cross-correlate the change in myosin intensity (myosin
548 intensity at a timepoint minus myosin intensity at the previous time point) with constriction
549 change (cell area at a timepoint minus cell area at the next time point, i.e. positive value if
550 constricting, negative if stretching) for each cell trace. Cross-correlations for each cell were
551 averaged by bin (distance from the midline) and plotted.

552 **Curvature analysis**

553 Movies with at least 20 μm z-depth were resliced in FIJI to create transverse virtual
554 cross sections (1 μm thickness) of the ventral furrow all along the embryo's AP axis. Apically
555 enriched myosin signal was used to trace the apical surface of the folding tissue with the
556 freehand line tool in Fiji. Traces were made for a cross section at the center of the AP axis of
557 the embryo as well as for cross-sections 20 μm anterior and posterior, respectively. The
558 timepoint of measurement was chosen based on invagination depth (about 10 μm). The XY
559 coordinates of each trace were imported into Matlab R2019a. After manually determining the
560 position of the ventral midline, a circle fit (Nikolai Chernov (2020). Circle Fit (Taubin method)
561 (https://www.mathworks.com/matlabcentral/fileexchange/22678-circle-fit-taubin-method),
562 MATLAB Central File Exchange. Retrieved February 5, 2020) was applied to the central part of
563 the trace, 2.5 μm left and right of the midline. The inverse of the fitted circle radius was defined
564 as the fold curvature. The three traces taken from each embryo were averaged to obtain the fold

565 curvature value for that embryo. In addition, local curvature was visualized using
566 LineCurvature2D (Dirk-Jan Kroon (2020). 2D Line Curvature and
567 Normals (https://www.mathworks.com/matlabcentral/fileexchange/32696-2d-line-curvature-and-
568 normals), MATLAB Central File Exchange. Retrieved March 16, 2020.) in Matlab.
569 Post-folding lumina were visualized from central cross-sections of the same embryos
570 whose curvature had been analyzed and measured for a single AP position. Lumen area was
571 determined by manually fitting an ellipse to the lumen in each cross-section in Fiji and
572 measuring its area.

573 Curvature and lumen measurements were compared between genotypes using the non-
574 parametric two-sample Mann-Whitney U test (‘ranksum‘ command in Matlab).

575 **Regression analysis**

576 All linear regression fits (Fig. 1 E, 7 D) were performed in Matlab R2019a using the fitlm
577 command. The original data as well as the best fit line were plotted and the R-squared value
578 was reported as a measure of fit.

579 For myosin gradients, the position of the most lateral bin with myosin levels above half-
580 maximal was used to describe gradient width. This bin position was then compared to central
581 curvature measurements of the same embryo at a later timepoint (at ~10 μm invagination depth,
582 analyzed with circlefit).

583

584

585 **Acknowledgments**

586 We thank N. Perrimon, L. Perkins and the Transgenic RNAi Project at Harvard Medical School
587 (National Institutes of Health/National Institutes of General Medical Sciences R01-GM084947) for
588 providing transgenic RNAi stocks. We thank V. Tserunyan for the software adapted here to analyze
589 myosin pulses. We thank B. Adhikary for help with analysis of F-actin levels. We thank current and
590 former Martin lab members for helpful discussions and feedback. This work was supported by a
591 grant from the National Institutes of General Medical Sciences: R01GM125846 to A.C.M.

592
593

594

595 **Figure legends**

596 **Figure 1.** Tissue-wide mesodermal F-actin distribution is distinct from Myosin. **(A)** Myosin
597 gradient extends 6 cells from the ventral midline (VM) and remains low. Images are apical
598 surface view of embryo labeled with sqh::GFP (Myosin) and Gap43::mCherry (membrane) and
599 segmented example of embryo with cell rows highlighted in different colors. Scale bar = 10 μm.
600 Colors in image correspond to bins in adjacent plots showing myosin intensity and apical area
601 distributions in a representative wild-type embryo. **(B)** Junctional F-actin is depleted in the
602 mesoderm prior to furrow formation. Images are apical shell projection (top) and cross-section
603 (bottom) image of phalloidin stained embryos imaged before furrow formation. Scale bar = 10
604 μm. Plot shows junctional F-actin density for cells of one embryo binned by position from ventral
605 midline. Data is represented by box-and-whisker plot from representative embryo, where bottom
606 and top sides of the box represent 25th and 75th percentile of cells, respectively. Midline is the
607 median and red '+' are outliers. n = at least 40 cells per bin (median 51.5 cells). **(C)** Junctional
608 F-actin accumulates in a ventral-lateral gradient during furrow formation. Images and plots are
609 analogous to (B). n = at least 15 cells per bin (median 73 cells). **(D)** Average F-actin density
610 trace for 3 embryos corresponding to (B) (pre-furrow) and (C) (furrow), normalized to the cell
611 row with the highest mean. Shaded area depicts 1 standard deviation in each direction. **(E)**
612 Apical area is anti-correlated with cortical F-actin levels. Quantification of cortical F-actin density
613 per cell (cortical levels normalized by perimeter) for the embryo shown in (C) was plotted as a
614 function of apical area. Color of data points represents physical distance from ventral midline in
615 μm. Average pre-fold cell area for fixed embryos (~16 μm^2 due to shrinkage during the fixation
616 process) is indicated with dotted grey line.
617

618 **Figure 2.** Snail and Twist regulate distinct features of the tissue-wide F-actin pattern. **(A)** Snail
619 expression boundary corresponds to F-actin depletion boundary. Images are from phalloidin-

620 stained embryo co-stained with anti-Snail. Cyan stars in F-actin image designate Snail-positive
621 cells bordering the ectoderm. Scale bar = 10 μm. **(B)** The *snail* mutant disrupts mesodermal F-
622 actin depletion. Images are subapical shell-projections from representative, live homozygous
623 *snail* mutant and normal sibling embryo expressing Utrophin::mCherry (F-actin). The *snail*
624 mutant shows a lack of F-actin patterning. Scale bar = 10 μm. **(C)** Quantification of junctional F-
625 actin density by cell row from 3 *snail* mutant and 3 normal sibling embryos (Mean and standard
626 deviation shown). All *snail* mutants lack F-actin patterning. All traces were normalized to their
627 highest-mean cell bin before averaging. Dotted black line designates approximate mesoderm-
628 ectoderm boundary in control embryos. **(D)** The *twist* mutant exhibits F-actin depletion, but lacks
629 F-actin elevation around midline. Images are subapical shell-projections from 3 representative,
630 live homozygous *twist* mutant and 3 normal sibling embryos expressing Utrophin::mCherry (F-
631 actin). Scale bar = 20 μm. **(E)** Quantification of junctional F-actin density from 3 *twist* mutant and
632 3 normal sibling embryos (Mean and standard deviation shown). All *twist* mutants exhibit F-actin
633 depletion, but not the increase around the midline. All traces were normalized to their highest-
634 mean cell bin before averaging. Dotted lines mark respective transitions from low-F-actin to high
635 F-actin regions of the tissue. **(F)** Average F-actin density and standard deviations overlaid for 3
636 *twist* and 3 *snail* mutant embryos. *twist* mutants display ventral F-actin depletion but *snail*
637 mutants do not.

638

639 **Figure 3.** Myosin gradient and uniform F-actin depletion do not require intercellular coupling. **(A)**
640 Images (apical shell projections) of control (Rh3-RNAi) and α-catenin-RNAi embryos expressing
641 sqh::GFP (Myosin, green) and Gap43::mCherry (Membranes, magenta). Scale bar = 10 μm. **(B)**
642 and **(C)** Quantification of apical area (magenta, **B**) and normalized apical, active myosin (green,
643 **C**) as a function of distance from ventral midline. Data is represented by box-and-whisker plots
644 where each bin is a cell row at a given distance from the ventral midline (n = at least 41 (control)

645 or 44 (α-catenin-RNAi) cells per row; median 72 (control) or 107 (α-catenin-RNAi) cells). Bottom
646 and top sides of the box represent 25th and 75th percentile, respectively. Midline is the median
647 and red points are outliers. **(D)** Images are phalloidin-stained control (Rh3-RNAi, top) and α-
648 catenin-RNAi (bottom) embryos focused on the mesoderm-ectoderm boundary. Scale bar = 10
649 μm. Plots are normalized junctional F-actin density in rows of cells along the ventral-lateral axis
650 (n= at least 52 (control) or 8 (α-catenin-RNAi) cells per row; median 78 (control) or 40.5 (α-
651 catenin-RNAi) cells). Data representation is same as (B) and (C). **(E)** Mean (+ standard
652 deviation) traces for several control and α-catenin-RNAi embryos. Top: Average apical area
653 behavior from 4 different embryos, per condition. Mid: Average apical myosin intensity behavior
654 from 4 different embryos, respectively. Bottom: Average junctional actin density from 3 different
655 embryos, respectively.
656
657 **Figure 4.** RhoA activation occurs in a gradient. **(A)** Simplified diagram of signaling downstream
658 of Twist, focused on RhoA regulation. **(B) Top**: Image of RhoGEF2::GFP, **Middle:** Image of
659 Anillin Rho-binding domain::GFP (Active RhoA), **Bottom:** Image of Rok::GFP, and
660 Gap43::mCherry (membranes). Ventral midline in center. Scale bar = 10 μm. Plots are
661 normalized apical RhoGEF2::GFP intensity (**top**), Anillin Rho-binding domain::GFP intensity
662 (**mid**), and Rok::GFP intensity (**bottom**) as a function of distance from the ventral midline for
663 one representative embryo, respectively. Data is represented by box-and-whisker plots where
664 each bin is a cell row at a given distance from the ventral midline. Bottom and top sides of the
665 box represent 25th and 75th percentile, respectively. Midline is the median and red points are
666 outliers. At least 32 cells (rhoGEF2, median 85 cells), 58 cells (Active RhoA, median 76.5 cells),
667 or 51 cells (Rock, median 68.5 cells) were analyzed for each cell row. Brightness and contrast
668 were adjusted individually to best display the intensity range for each marker. **(C)** Average (+
669 standard deviation) fluorescent signal across cell rows for 5 (RhoGEF2::GFP, Rok::GFP) or 4

670 (Anillin Rho-binding domain::GFP) embryos, respectively. Traces are normalized to highest-
671 mean cell row, respectively.
672
673 **Figure 5:** RhoA overactivation widens actomyosin gradient and elevates F-actin at the
674 mesoderm margin. **(A-B)** Images (apical shell projections) of control (Rh3-RNAi) and C-GAP-
675 RNAi embryos **(A)** expressing two copies of sqh::GFP (Myosin, green) and Gap43::mCherry
676 (Membranes, magenta), or control and RhoGEF2 O/E embryos **(B)** expressing one copy of
677 sqh::GFP (Myosin, green) and Gap43::mCherry (Membranes, magenta). Scale bars = 10 μm.
678 **(C-D)** C-GAP-RNAi and RhoGEF2 O/E embryos have a wider half-maximal gradient position.
679 **Left:** Average (+ standard deviation) normalized myosin intensity (top) and apical area (bottom)
680 behavior for **(C)** control (n = 4 embryos) and C-GAP RNAi (n = 5 embryos) or **(D)** control (n = 4
681 embryos) and RhoGEF2 O/E (n = 7 embryos). Dashed lines indicate half-maximal myosin and
682 unconstricted apical area, respectively. Control embryos for (C) are the same as in Fig. 3 E.
683 **Right:** Quantification of normalized apical, active myosin (green, **top**) and apical area
684 (magenta, **bottom**) as a function of distance from ventral midline for a single C-GAP-RNAi (C)
685 or RhoGEF2 O/E embryo (D). Data is represented by box-and-whisker plots where each bin is a
686 cell row at a given distance from the ventral midline (n= at least 50 cells/row (C) or 23 cells/row
687 (D); median 108.5 cells (C) and 85 cells (D)). Bottom and top sides of the box represent 25th
688 and 75th percentile, respectively. Midline is the median and red points are outliers. **(E** and **G)**
689 Images (subapical shell projection) of control (Rh3-RNAi), C-GAP-RNAi, or RhoGEF2-RNAi
690 embryos (E) or RhoGEF2 O/E embryo (G) expressing Utrophin::GFP. Scale bars = 10 μm. **(F**
691 and **H)** RhoA activity affects junctional F-actin density in cells at the mesoderm margin. **Top:**
692 Average F-actin density behavior (and standard deviation) from different embryos, normalized to
693 mean of highest cell row, for **(F)** control RNAi (n=3), C-GAP-RNAi (n=3), and RhoGEF2-RNAi
694 (n=3) or **(H)** control RNAi (n=2), RhoGEF2 O/E (n=5). **Mid:** Quantification of normalized
695 subapical F-actin density as a function of distance from ventral midline for a single C-GAP-RNAi

696 **(F)** or RhoGEF2 O/E **(H)** embryo (n= at least 9 cells/row (F and H); median 25.5 cells (F) and
697 21.5 cells (H)). Data representation same as (C) and (D). **Bottom:** Quantification of normalized
698 subapical F-actin density as a function of distance from ventral midline for a single RhoGEF2-
699 RNAi embryo (n= at least 11 cells/row; median 15 cells).
700
701 **Figure 6:** Contractile dynamics vary with distance from ventral midline. **(A)** Diagram
702 categorizing types of dynamic cell behaviors during ventral furrow formation. Top: When RhoA
703 activity is high, cells preferably undergo "ratcheted" pulses after which a higher myosin
704 constriction level is maintained than before the pulse. At moderate RhoA activity, cells
705 preferably undergo reversible pulses in which myosin and constriction levels are similar to
706 before the pulse. **(B-C)** Average and standard error of myosin dynamics **(B)** and apical area
707 dynamics **(C)** around pulses (local maxima in myosin accumulation rate) for cell row 1 at the
708 midline, cell row 4 within the myosin gradient and marginal mesoderm cell row 7 shown for one
709 representative embryo. 106 pulses were analyzed for cell row 1; 192 pulses were analyzed for
710 cell row 4; 335 pulses were analyzed for cell row 7. **(D)** Average and standard error for
711 persistence of myosin (minimum myosin 0-100 s after pulse - minimum myosin 0-100 s before
712 pulse) and area (maximum area 0-100 s after pulse - maximum area 0-100 s before pulse) by
713 bin (distance from the midline) for three embryos. At least 83 pulses were analyzed for each cell
714 row in each embryo. Median 192, 238 and 343 pulses analyzed per cell row for the three
715 embryos, respectively. **(E)-(G)** Top: Cross-correlation of myosin rate and constriction rate
716 averaged by cell bin; split up by ventral mesoderm (cell rows 1-5, **E**), marginal mesoderm (cell
717 rows 7-9, **F**) and ectoderm (cell rows 11 and 12, **G**). At least 21 cells per cell row were
718 analyzed, median 32 cells per cell row. Bottom: Myosin (green) and apical area (magenta)
719 traces (normalized to average) and images of representative individual cells during a myosin
720 pulse, for each region. Scale bars = 2 μm.
721

722 **Figure 7:** The contractile gradient width affects furrow curvature and post-fold shape. **(A** and **B)**
723 Cross-sectional reslices during and after folding of control (Rh3-RNAi) and C-GAP-RNAi **(A)** or
724 RhoGEF2 O/E **(B)** embryos expressing sqh::GFP (myosin) and gap43::mCherry (membranes).
725 In control embryos, the ventral-lateral cross-section shows a narrow, v-shaped fold with high
726 curvature at the center (local curvature is color-coded on the surface of the fold). The cross-
727 sectional view of the same embryo at a later timepoint shows a tube with a very small lumen. C-
728 GAP-RNAi and RhoGEF2 O/E embryos, which have a widened gradient, display lower central
729 fold curvature and an enlarged tube lumen. Scale bars = 10 μm. Images were rotated to orient
730 ventral side up and black pixels added at corners. **(C-D)** Quantification of curvature at the center
731 of the fold (measured by fitting a circle, three measurements averaged per embryo, C) and
732 lumen size (measured by fitting an ellipse, D) for C-GAP-RNAi and RhoGEF2 O/E embryos with
733 respective controls. Data is represented by box-and-whisker plots overlaid with data points
734 representing each quantified embryo. Bottom and top sides of the box represent 25th and 75th
735 percentile of embryos, respectively. Red midline is the median. P-values are based on pairwise
736 comparison with Mann-Whitney U test. **(E)** Regression analysis of the relationship between
737 myosin gradient width and curvature for control, C-GAP-RNAi and RhoGEF2 O/E embryos.
738 Gradient width was determined as the most lateral bin with mean intensity higher than half-
739 maximal. Curvature was measured as in (C). **(F)** Model for the regulation of tissue-wide
740 patterning in the ventral furrow. Uniform *snail* expression causes uniform F-actin depletion in the
741 mesoderm. Overlapping graded expression of *twist* targets acts via RhoA activation to generate
742 an actomyosin gradient. Fold curvature is driven by the combination of midline contractility and
743 marginal stretching.
744
745
746
747

748

749 **Supplemental Figure 1.** F-actin is depleted in the mesoderm during cellularization. **(A)** F-actin
750 depletion in the mesoderm appears towards the end of cellularization. Images are subapical
751 shell projections (top) and cross-sections (bottom) of wild-type embryos at different stages
752 stained with phalloidin (red) and anti-snail antibody (cyan). Scale bars = 10 μm. Cross-sectional
753 images were rotated to orient ventral side up and black pixels added at corners. Brightness and
754 contrast were adjusted individually to best display the intensity range in each image. **(B)**
755 Integrated junctional F-actin intensity per cell before and after folding (mean and standard
756 deviation, for same embryos as Figure 1 D). Mean junctional F-actin intensity was calculated by
757 segmenting cells and integrating F-actin intensity around the cell periphery. All traces were
758 normalized to their highest-mean cell bin before averaging. **(C)** Mean subapical F-actin
759 junctional density by cell row over time for a single embryo marked with Utrophin::GFP, from
760 mid-cellularization (0 min) to during folding (20.5 min). F-actin density stays mostly constant in
761 the ectoderm, but decreases in the mesoderm during cellularization and then increases in a
762 gradient around the ventral midline. **(D)** Left: F-actin marked by the fluorescently marked
763 Utrophin::GFP (cyan) is depleted in the marginal mesoderm, but a general membrane marker,
764 Gap43::mCherry (red), is not. Images show both markers in subapical shell projections
765 (gaussian blur radius=1) and cross-sections. Scale bar = 10 μm. Right: Quantification by bin of
766 subapical Utrophin::GFP (top) and Gap43::mCherry (bottom) junctional fluorescent intensity,
767 normalized by perimeter. Data is represented by box-and-whisker plots where each bin is a cell
768 row at a given distance from the ventral midline (at least 21 cells per row analyzed, median 38
769 cells). Bottom and top sides of the box represent 25th and 75th percentile junctional intensity per
770 cell, respectively. Midline is the median and red points are outliers.

771

772 **Supplemental Figure 2.** Workflow for subapical shell projections in FIJI. Confocal image stacks
773 are resliced along the ventral-lateral axis to get a cross-sectional view. A subapical trace is then

774 drawn manually and the embryo is resliced a second time along the trace. The central part of
775 the embryo along the AP axis is then used to segment cells and quantify intensity along the
776 ventral-lateral axis.
777
778 **Supplemental Figure 3:** F-actin is colocalized with junctions in wild-type and with medioapical
779 myosin spots in α -catenin-RNAi. **(A)** Top: apical shell projection images of fixed control RNAi
780 embryo stained with phalloidin (red) and anti-E-cadherin antibody (cyan). Bottom: Cross-section
781 images of fixed wild-type embryo stained with phalloidin (red) and anti-E-cadherin antibody
782 (cyan). Yellow arrows mark mesoderm-ectoderm border. Scale bars = 10 μm. Cross-sectional
783 images were rotated to orient ventral side up and black pixels added at corners. **(B)** Images of
784 ventral apical surface of fixed embryo expressing sqh::GFP (Myosin light chain marker), stained
785 with phalloidin (red) and anti-GFP (cyan) antibody (same embryo as in Figure 3 D). Yellow
786 arrows indicate medioapical spots in which myosin and F-actin are colocalized. Scale bar = 10
787 μm.
788
789 **Supplemental Figure 4.** C-GAP is uniformly cytoplasmic across the ventral furrow. **(A)** Apical
790 shell projection of an embryo expressing GFP::C-GAP (green) and gap43::mCherry
791 (membranes, magenta). White arrows indicate apical nucleus with no GFP::C-GAP signal.
792 Scale bar = 10 μm.
793
794 **Supplemental Figure 5:** C-GAP-RNAi expands the active RhoA zone and RhoGEF2-RNAi
795 decreases myosin levels, but there is still a gradient**. (A)** Images (apical shell projection) of
796 control (Rh3-RNAi) and C-GAP-RNAi embryos expressing Anillin Rho-binding domain::GFP
797 (active RhoA, yellow) and Gap43::mCherry (Membranes, magenta). Scale bar = 10 μm. **(B)**
798 Top: Image (apical shell projection) of RhoGEF2-RNAi embryo expressing sqh::GFP (Myosin,
799 green) and Gap43::mCherry (Membranes, magenta). Scale bar = 10 μm. Bottom: Quantification

800 of apical area (magenta) and normalized apical, active myosin (green) as a function of distance
801 from ventral midline (at least 23 cells per cell row were analyzed; median 38 cells). Data is
802 represented by box-and-whisker plots where each bin is a cell row at a given distance from the
803 ventral midline. Bottom and top sides of the box represent 25th and 75th percentile of cells,
804 respectively. Midline is the median and red points are outliers. Inset shows average cell
805 behavior (and standard deviation) from 5 different RhoGEF2-RNAi and 4 different control
806 embryos. Short hairpin RNAs were driven by Mat 67 and 15 Gal4 drivers. Control embryos are
807 the same as in Figure 5 D.
808
809
810 **Supplemental Figure 6:** Junctional F-actin levels in the marginal mesoderm affect fold
811 curvature. **(A) Top:** Cross-sections during folding of RhoGEF2-RNAi, control (Rh3-RNAi) and C-
812 GAP-RNAi embryos expressing Utrophin-GFP. In cross-section, local curvature is color-coded
813 on the surface of the fold. Scale bars = 10 μm. Bottom: Cross-sections during folding of control
814 (Rh3-RNAi) and RhoGEF2 O/E embryos expressing Utrophin-GFP. Images were rotated to
815 orient ventral side up and black pixels added at corners. **(B)** Quantification of curvature at the
816 center of the fold (measured by fitting a circle, three measurements averaged per embryo) for
817 control (Rh3-RNAi), RhoGEF2-RNAi, control (Rh3-RNAi) and C-GAP-RNAi, as well as control
818 (Rh3-RNAi) and RhoGEF2 O/E embryos. Maternal GAL4 drivers used to drive short-hairpin
819 RNAs or RhoGEF2 are indicated. Data is represented by box-and-whisker plots overlaid with
820 data points from all quantified embryo. Bottom and top sides of the box represent 25th and 75th
821 percentile, respectively. Midline is the median. P-values are based on pairwise comparisons
822 with Mann-Whitney U test.
823
824

825 **Supplemental Movie S1 (related to Fig. 4).** Shell-projection (with background subtraction
826 and gaussian blur) of control (Rh3-RNAi) embryo expressing sqh::GFP (myosin) and
827 gap43::mCherry (membranes) during ventral furrow formation.
828
829 **Supplemental Movie S2 (related to Fig. 4).** Shell-projection (with background subtraction
830 and gaussian blur) of α-catenin-RNAi embryo expressing sqh::GFP (myosin) and
831 gap43::mCherry (membranes) trying to initiate ventral furrow formation.
832
833
834 **Supplemental Movie S3 (related to Fig. 7).** Maximum intensity projection (38 μm depth) of
835 control (Rh3-RNAi) embryo expressing sqh::GFP (myosin) and gap43::mCherry (membranes),
836 during and after ventral furrow formation.
837
838 **Supplemental Movie S4 (related to Fig. 7).** Maximum intensity projection (38 μm depth) of
839 RhoGEF2-RNAi embryo expressing sqh::GFP (myosin) and gap43::mCherry (membranes),
840 during and after ventral furrow formation. Note divisions of mitotic domain 10 visible at the
841 embryo surface after folding.

Figure 1

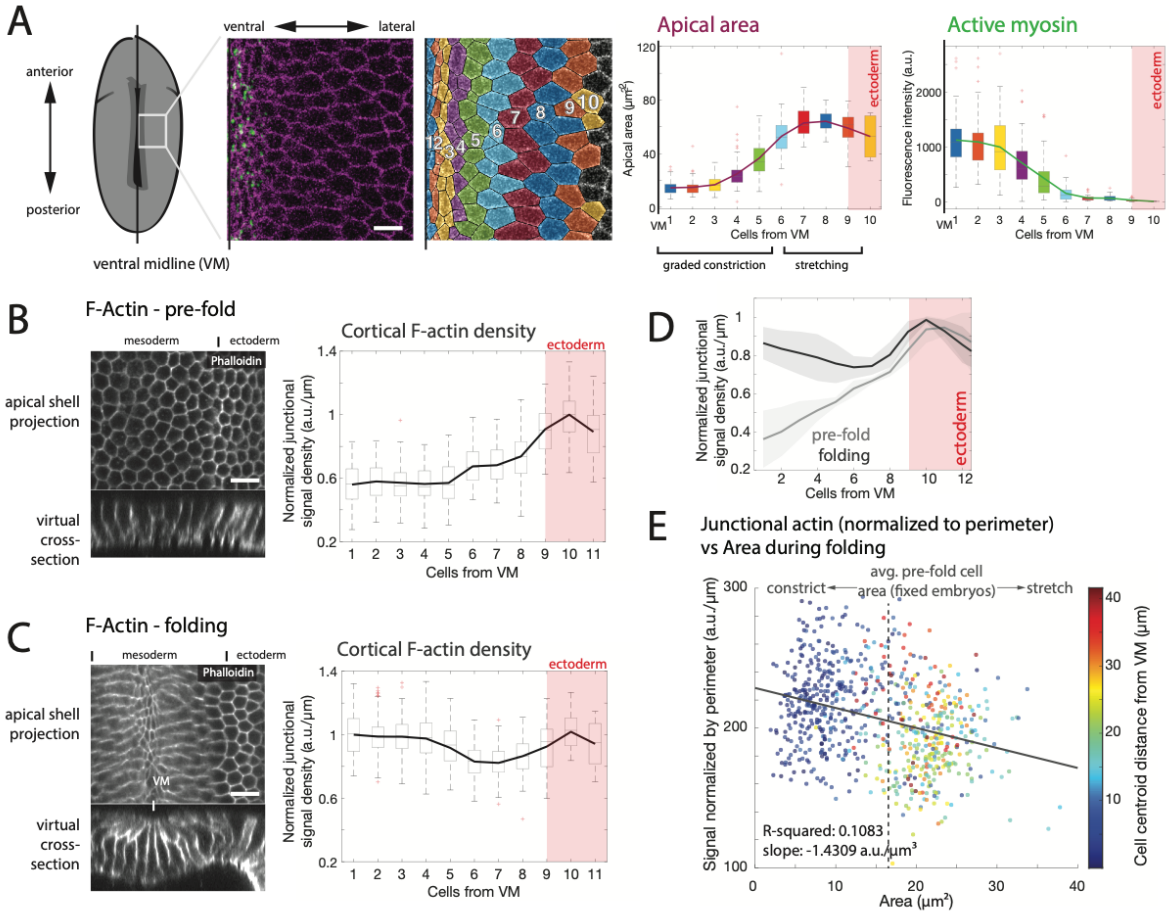
A
anterior
posterior
ventral
lateral
ventral midline (VM)
Apical area
Active myosin
Apical area (μm²)
Fluorescence intensity (a.u.)
Cells from VM
ectoderm
graded constriction
stretching
B
F-Actin - pre-fold
mesoderm
ectoderm
Phalloidin
apical shell projection
virtual cross-section
Cortical F-actin density
Normalized junctional signal density (a.u./μm)
C
F-Actin - folding
VM
D
pre-fold folding
E
Junctional actin (normalized to perimeter) vs Area during folding
avg. pre-fold cell area (fixed embryos)
constrict
stretch
Signal normalized by perimeter (a.u./μm)
Area (μm²)
Cell centroid distance from VM (μm)
R-squared: 0.1083
slope: -1.4309 a.u./μm³

844 Figure 2

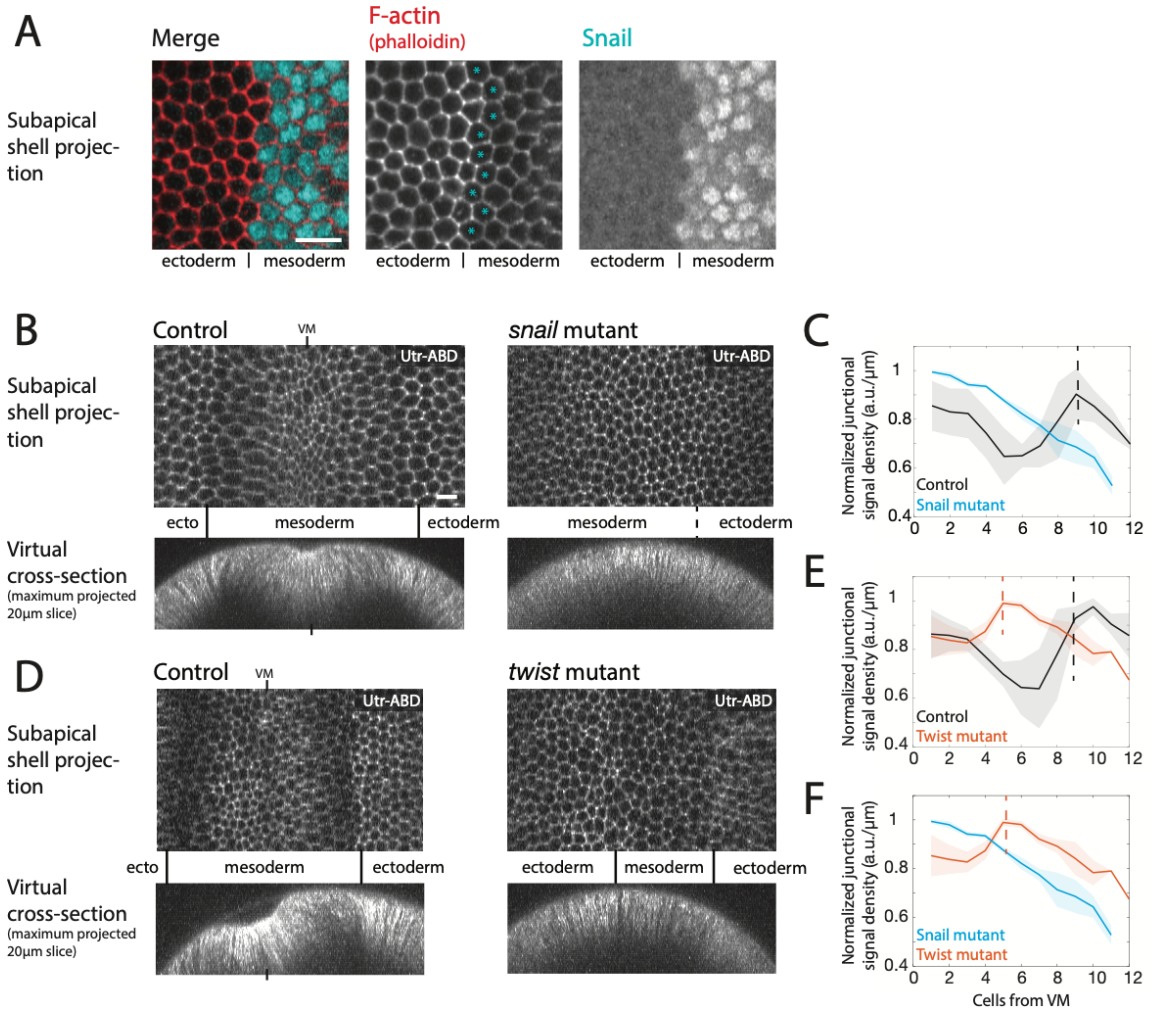

845

846 Figure 3

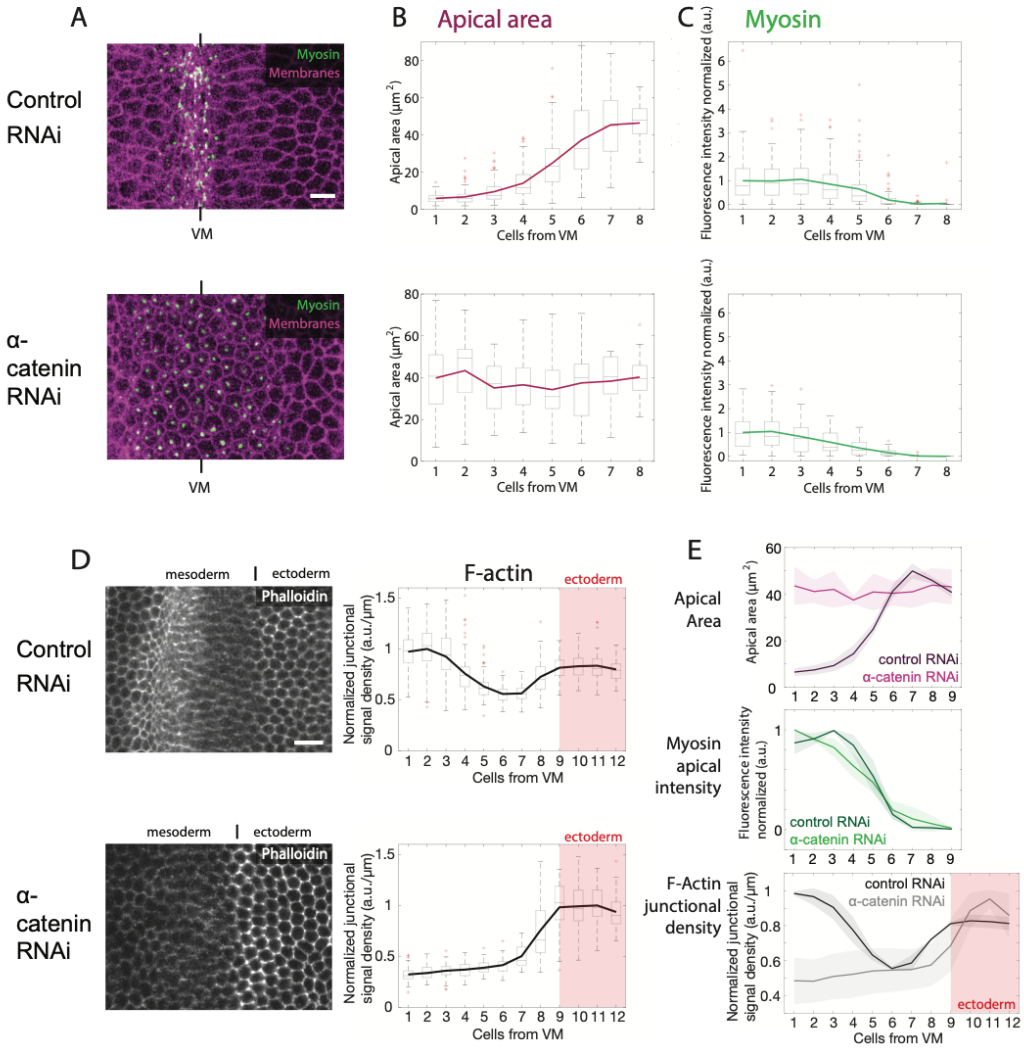

847

848 Figure 4

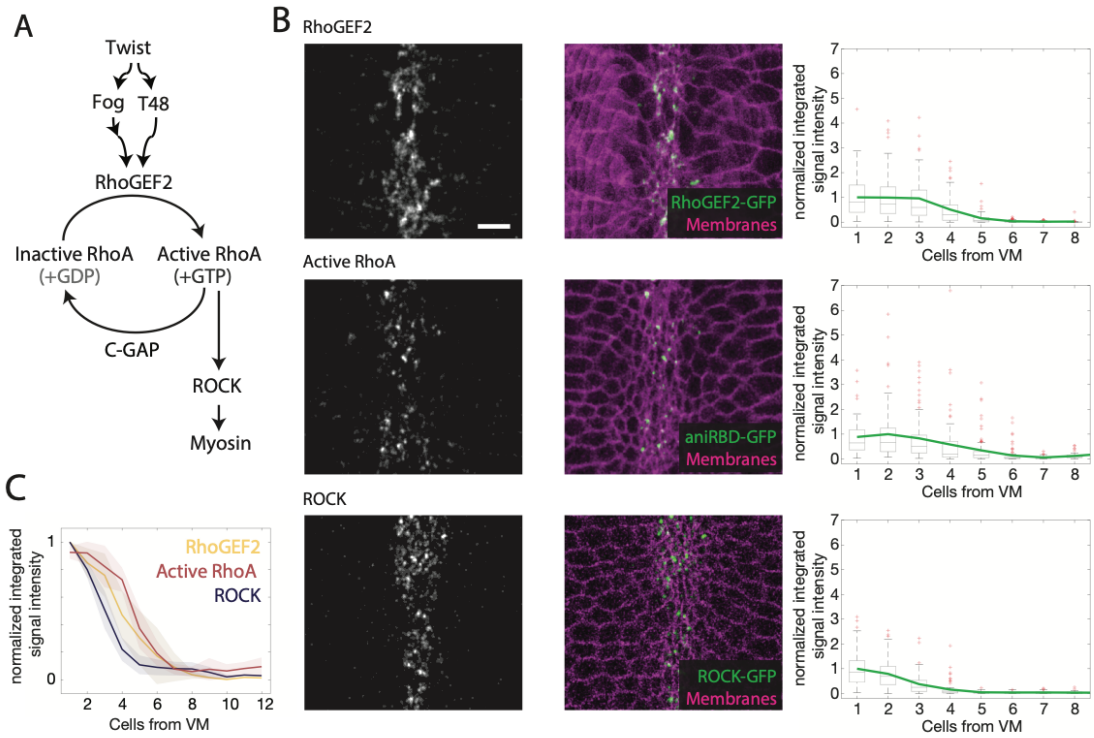

849

850 Figure 5

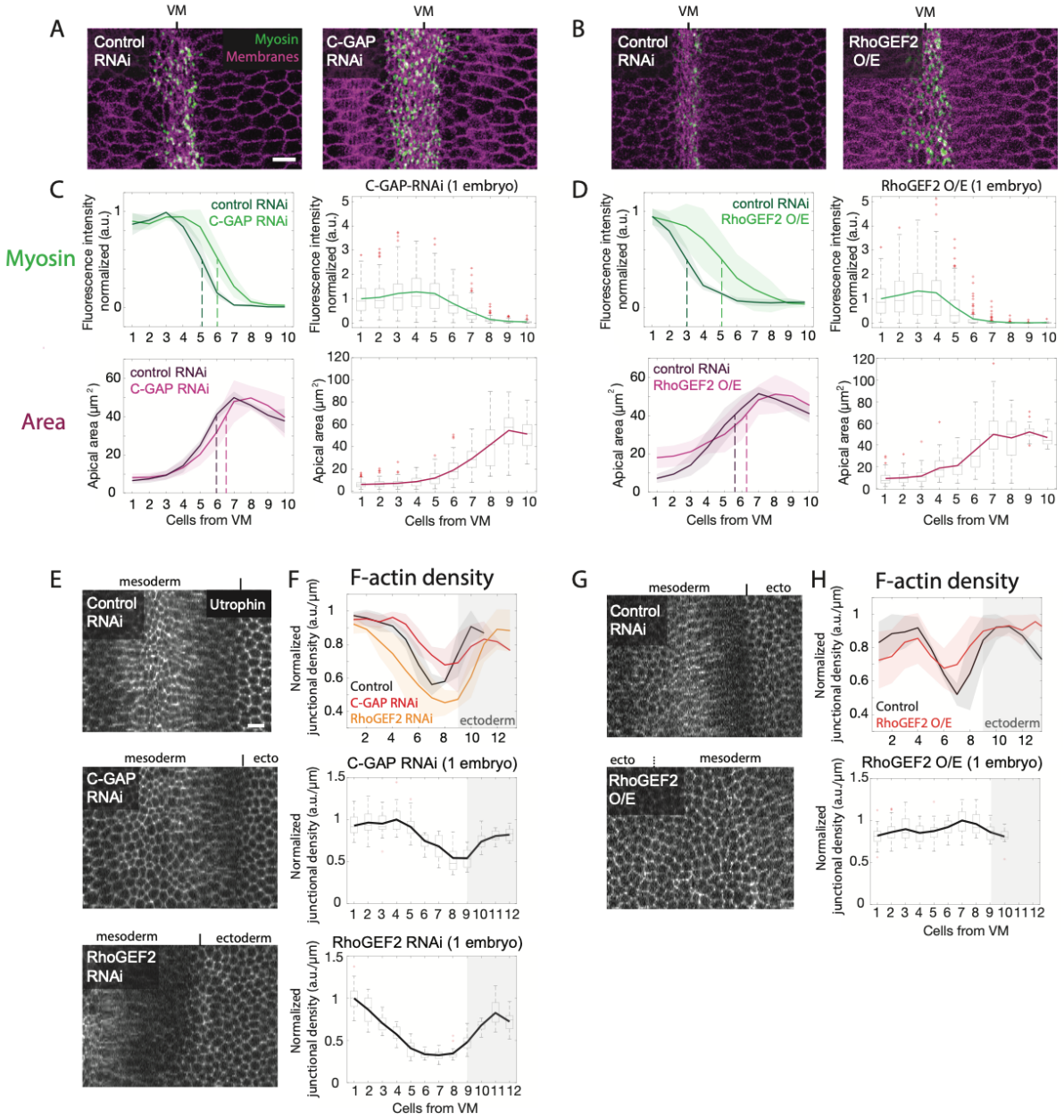

851

852 Figure 6

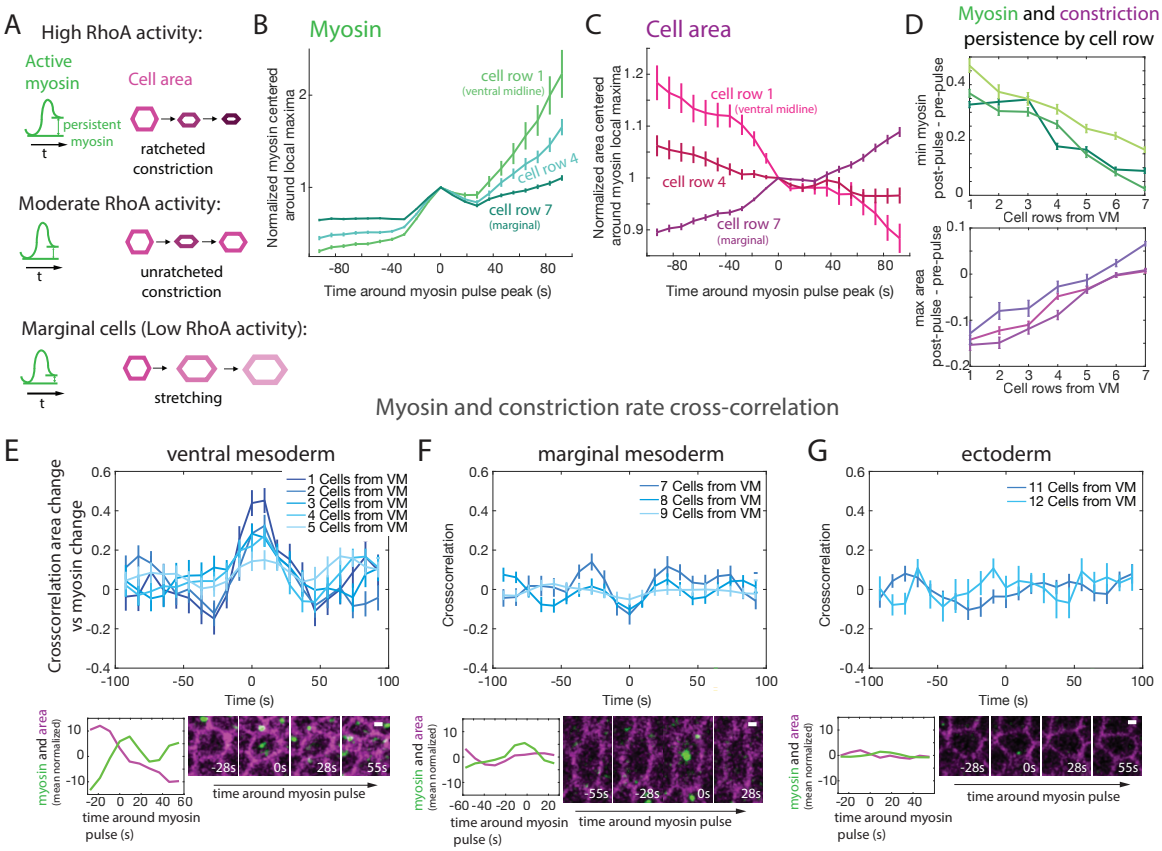

853

854 Figure 7

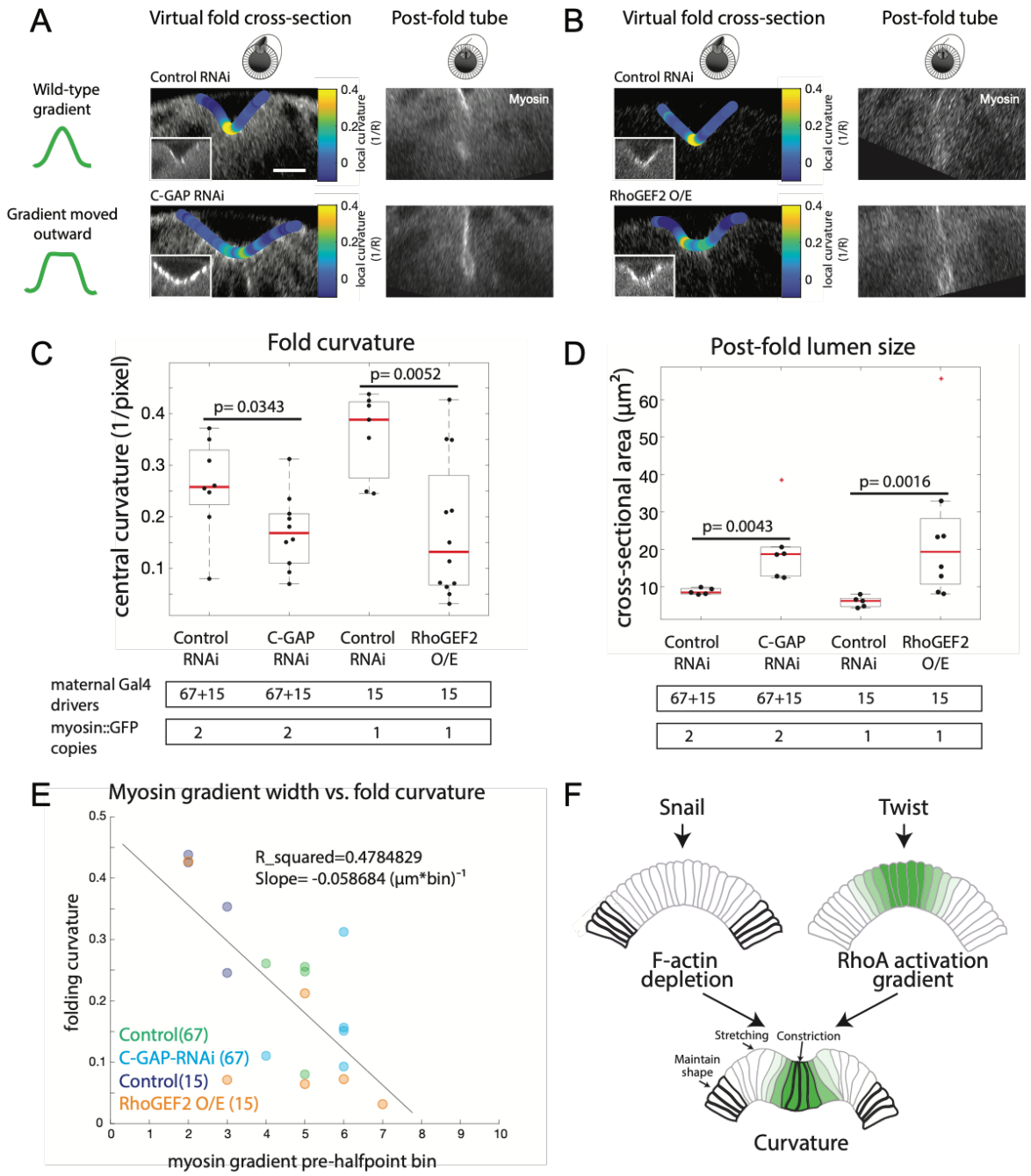

855

856 Supplemental Figure 1

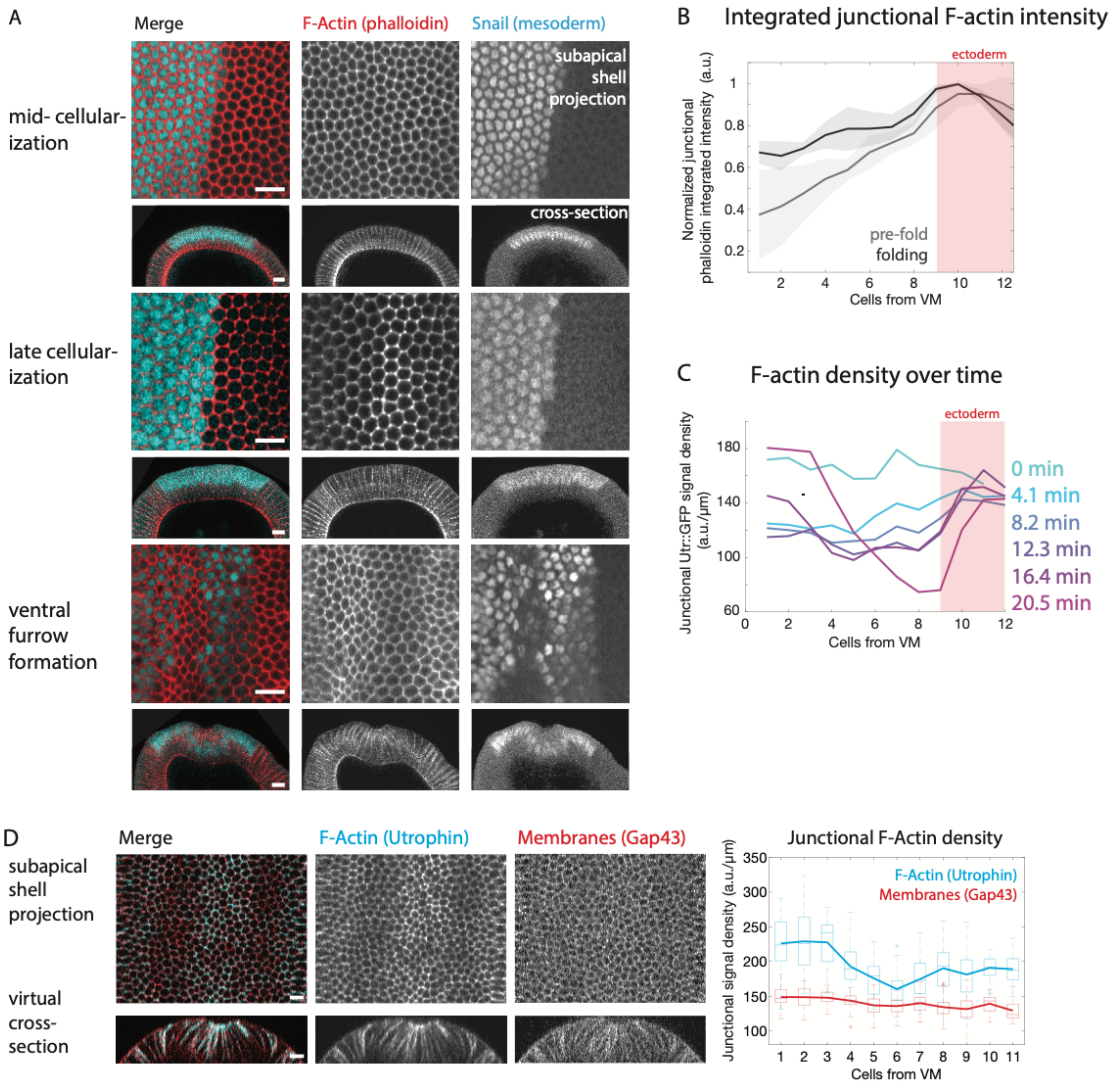

857

858 Supplemental Figure 2

Workflow for subapical shell projections:

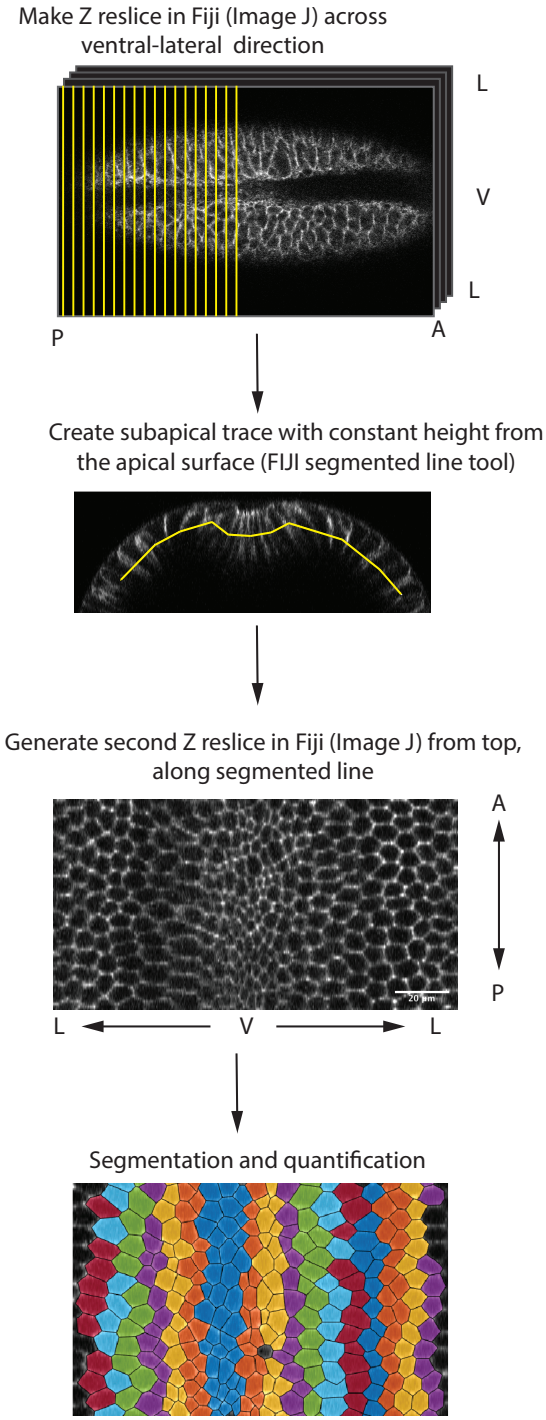

859

860 Supplemental Figure 3

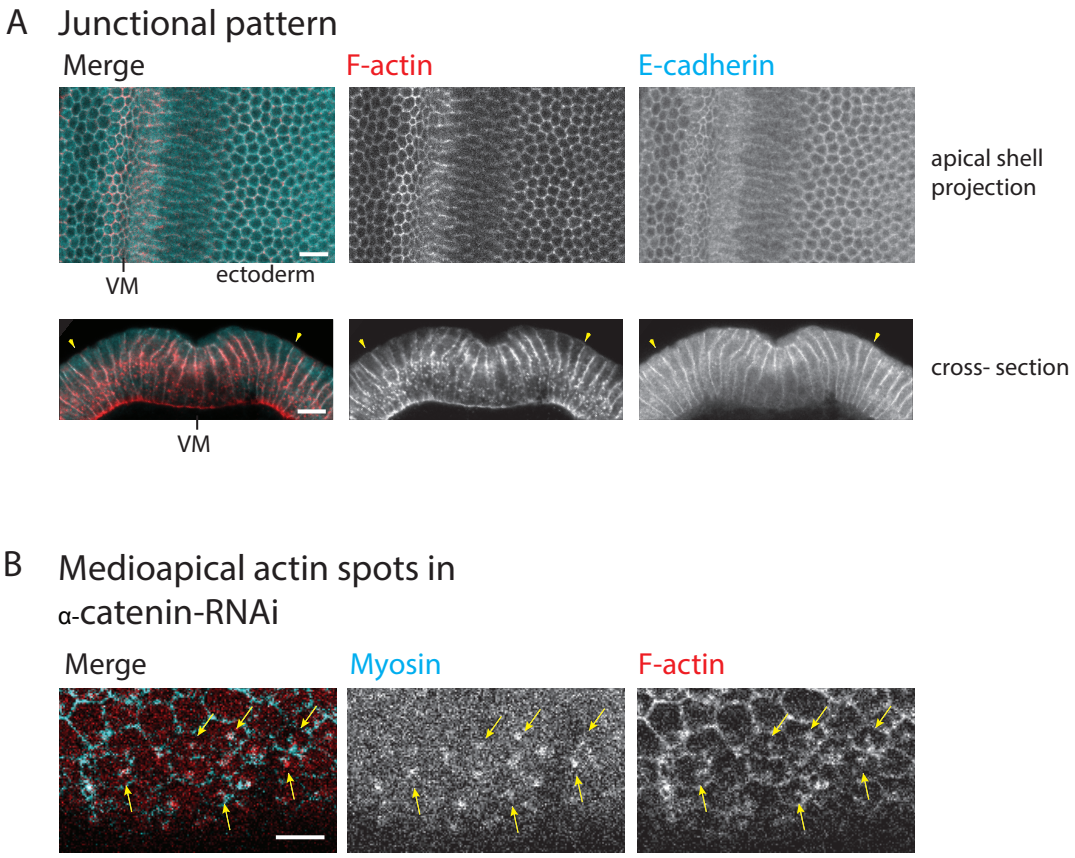

861

Supplemental Figure 4

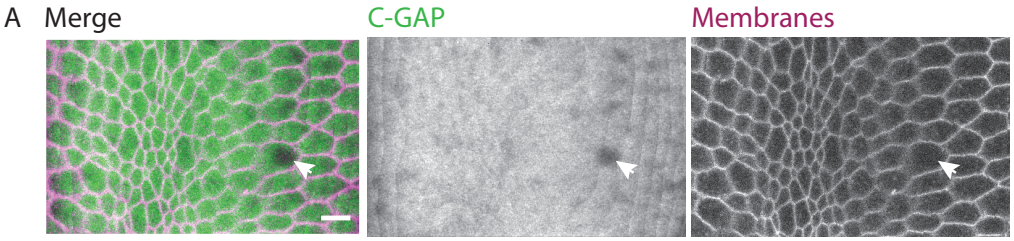

Supplemental Figure 5

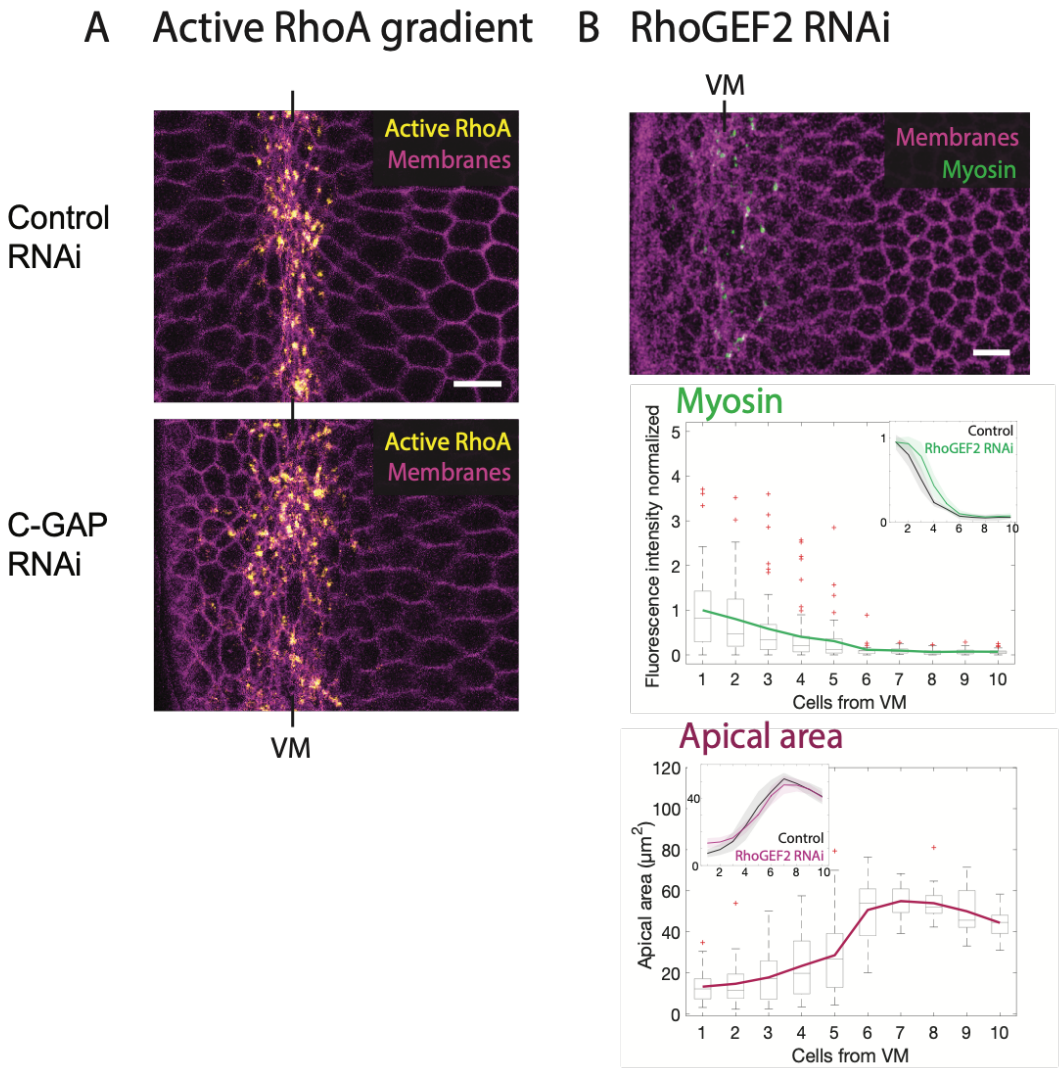

866 Supplemental Figure 6

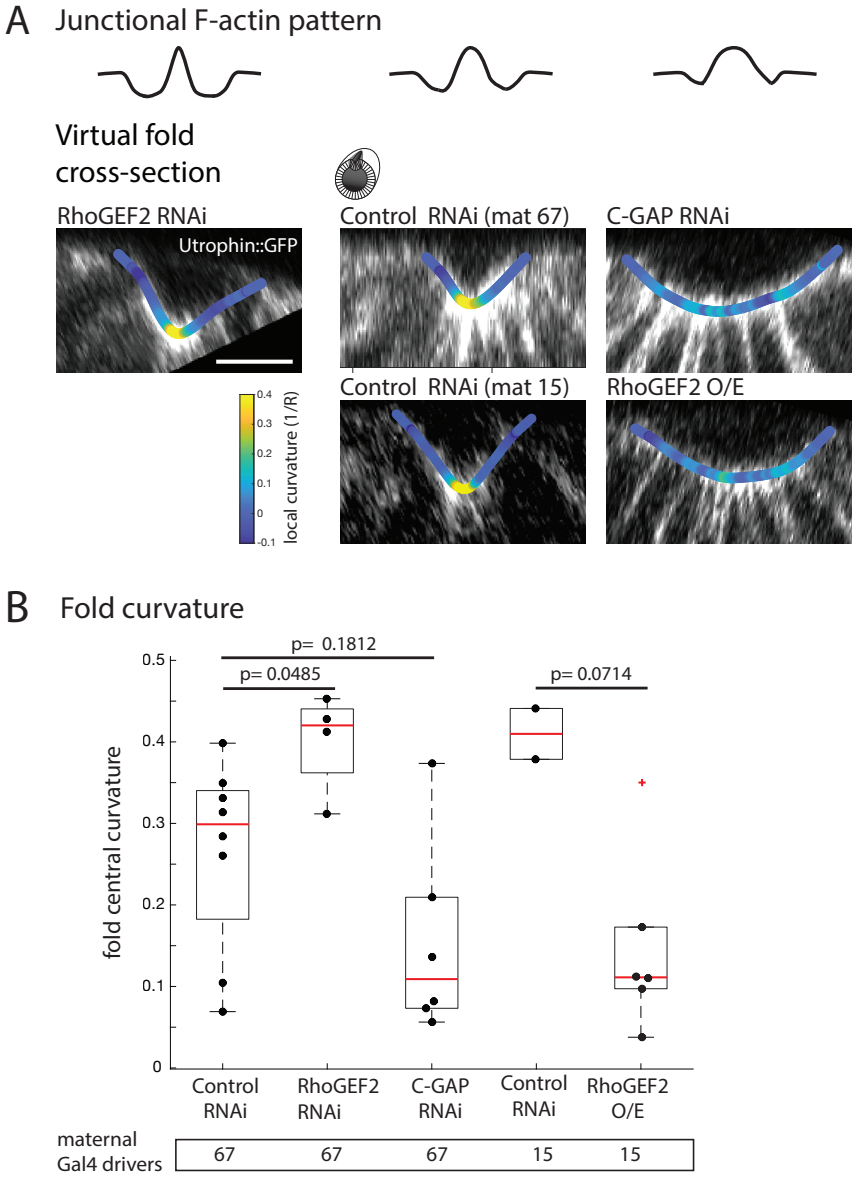

867

868 **References**

869

870 Bailles, A., C. Collinet, J.M. Philippe, P.F. Lenne, E. Munro, and T. Lecuit. 2019. Genetic
871 induction and mechanochemical propagation of a morphogenetic wave. *Nature*. 572:467-
872 473.
873 Barrett, K., M. Leptin, and J. Settleman. 1997. The Rho GTPase and a putative RhoGEF mediate
874 a signaling pathway for the cell shape changes in Drosophila gastrulation. *Cell*. 91:905-
875 915.
876 Boulay, J.L., C. Dennefeld, and A. Alberga. 1987. The Drosophila developmental gene snail
877 encodes a protein with nucleic acid binding fingers. *Nature*. 330:395-398.
878 Chanet, S., C.J. Miller, E.D. Vaishnav, B. Ermentrout, L.A. Davidson, and A.C. Martin. 2017.
879 Actomyosin meshwork mechanosensing enables tissue shape to orient cell force. *Nat*
880 *Commun*. 8:15014.
881 Chanet, S., and F. Schweisguth. 2012. Regulation of epithelial polarity by the E3 ubiquitin ligase
882 Neuralized and the Bearded inhibitors in Drosophila. *Nat Cell Biol*. 14:467-476.
883 Clement, R., B. Dehapiot, C. Collinet, T. Lecuit, and P.F. Lenne. 2017. Viscoelastic Dissipation
884 Stabilizes Cell Shape Changes during Tissue Morphogenesis. *Curr Biol*. 27:3132-3142.
885 Costa, M., E.T. Wilson, and E. Wieschaus. 1994. A putative cell signal encoded by the folded
886 gastrulation gene coordinates cell shape changes during Drosophila gastrulation. *Cell*.
887 76:1075-1089.
888 Dawes-Hoang, R.E., K.M. Parmar, A.E. Christiansen, C.B. Phelps, A.H. Brand, and E.F.
889 Wieschaus. 2005. folded gastrulation, cell shape change and the control of myosin
890 localization. *Development*. 132:4165-4178.
891 Denk-Lobnig, M., and A.C. Martin. 2019. Modular regulation of Rho family GTPases in
892 development. *Small GTPases*. 10:122-129.
893 Fernandez-Gonzalez, R., and J.A. Zallen. 2011. Oscillatory behaviors and hierarchical assembly
894 of contractile structures in intercalating cells. *Phys Biol*. 8:045005.
895 Foe, V.E. 1989. Mitotic domains reveal early commitment of cells in Drosophila embryos.
896 *Development*. 107:1-22.
897 Fox, D.T., and M. Peifer. 2007. Abelson kinase (Abl) and RhoGEF2 regulate actin organization
898 during cell constriction in Drosophila. *Development*. 134:567-578.
899 Furlong, E.E., E.C. Andersen, B. Null, K.P. White, and M.P. Scott. 2001. Patterns of gene
900 expression during Drosophila mesoderm development. *Science*. 293:1629-1633.
901 Fuse, N., F. Yu, and S. Hirose. 2013. Gprk2 adjusts Fog signaling to organize cell movements in
902 Drosophila gastrulation. *Development*. 140:4246-4255.
903 Gelbart, M.A., B. He, A.C. Martin, S.Y. Thiberge, E.F. Wieschaus, and M. Kaschube. 2012.
904 Volume conservation principle involved in cell lengthening and nucleus movement
905 during tissue morphogenesis. *Proc Natl Acad Sci U S A*. 109:19298-19303.
906 Gratz, S.J., M.M. Harrison, J. Wildonger, and K.M. O'Connor-Giles. 2015. Precise Genome
907 Editing of Drosophila with CRISPR RNA-Guided Cas9. *Methods Mol Biol*. 1311:335-
908 348.
909 Gratz, S.J., F.P. Ukken, C.D. Rubinstein, G. Thiede, L.K. Donohue, A.M. Cummings, and K.M.
910 O'Connor-Giles. 2014. Highly specific and efficient CRISPR/Cas9-catalyzed homology-
911 directed repair in Drosophila. *Genetics*. 196:961-971.
912 Grosshans, J., and E. Wieschaus. 2000. A genetic link between morphogenesis and cell division
913 during formation of the ventral furrow in Drosophila. *Cell*. 101:523-531.

914 Hacker, U., and N. Perrimon. 1998. DRhoGEF2 encodes a member of the Dbl family of
915 oncogenes and controls cell shape changes during gastrulation in Drosophila. *Genes Dev*.
916 12:274-284.
917 Heer, N.C., P.W. Miller, S. Chanet, N. Stoop, J. Dunkel, and A.C. Martin. 2017. Actomyosin-
918 based tissue folding requires a multicellular myosin gradient. *Development*. 144:1876-
919 1886.
920 Homem, C.C., and M. Peifer. 2008. Diaphanous regulates myosin and adherens junctions to
921 control cell contractility and protrusive behavior during morphogenesis. *Development*.
922 135:1005-1018.
923 Hong, L., M. Dumond, S. Tsugawa, A. Sapala, A.L. Routier-Kierzkowska, Y. Zhou, C. Chen, A.
924 Kiss, M. Zhu, O. Hamant, R.S. Smith, T. Komatsuzaki, C.B. Li, A. Boudaoud, and A.H.
925 Roeder. 2016. Variable Cell Growth Yields Reproducible OrganDevelopment through
926 Spatiotemporal Averaging. *Dev Cell*. 38:15-32.
927 Iseli, C., G. Ambrosini, P. Bucher, and C.V. Jongeneel. 2007. Indexing strategies for rapid
928 searches of short words in genome sequences. *PLoS One*. 2:e579.
929 Jha, A., T.S. van Zanten, J.M. Philippe, S. Mayor, and T. Lecuit. 2018. Quantitative Control of
930 GPCR Organization and Signaling by Endocytosis in Epithelial Morphogenesis. *Curr*
931 *Biol*. 28:1570-1584 e1576.
932 Jodoin, J.N., J.S. Coravos, S. Chanet, C.G. Vasquez, M. Tworoger, E.R. Kingston, L.A. Perkins,
933 N. Perrimon, and A.C. Martin. 2015. Stable Force Balance between Epithelial Cells
934 Arises from F-Actin Turnover. *Dev Cell*. 35:685-697.
935 Kerridge, S., A. Munjal, J.M. Philippe, A. Jha, A.G. de las Bayonas, A.J. Saurin, and T. Lecuit.
936 2016. Modular activation of Rho1 by GPCR signalling imparts polarized myosin II
937 activation during morphogenesis. *Nat Cell Biol*. 18:261-270.
938 Ko, C.S., P. Kalakuntla, and A.C. Martin. 2020. Apical Constriction Reversal upon Mitotic Entry
939 Underlies Different Morphogenetic Outcomes of Cell Division. *Mol Biol*
940 *Cell*:mbcE19120673.
941 Kolsch, V., T. Seher, G.J. Fernandez-Ballester, L. Serrano, and M. Leptin. 2007. Control of
942 Drosophila gastrulation by apical localization of adherens junctions and RhoGEF2.
943 *Science*. 315:384-386.
944 Latorre, E., S. Kale, L. Casares, M. Gomez-Gonzalez, M. Uroz, L. Valon, R.V. Nair, E. Garreta,
945 N. Montserrat, A. Del Campo, B. Ladoux, M. Arroyo, and X. Trepat. 2018. Active
946 superelasticity in three-dimensional epithelia of controlled shape. *Nature*. 563:203-208.
947 Leptin, M. 1991. twist and snail as positive and negative regulators during Drosophila mesoderm
948 development. *Genes Dev*. 5:1568-1576.
949 Leptin, M. 2005. Gastrulation movements: the logic and the nuts and bolts. *Dev Cell*. 8:305-320.
950 Leptin, M., and B. Grunewald. 1990. Cell shape changes during gastrulation in Drosophila.
951 *Development*. 110:73-84.
952 Lim, B., M. Levine, and Y. Yamazaki. 2017. Transcriptional Pre-patterning of Drosophila
953 Gastrulation. *Curr Biol*. 27:610.
954 Manning, A.J., K.A. Peters, M. Peifer, and S.L. Rogers. 2013. Regulation of epithelial
955 morphogenesis by the G protein-coupled receptor mist and its ligand fog. *Sci Signal*.
956 6:ra98.
957 Martin, A.C., M. Gelbart, R. Fernandez-Gonzalez, M. Kaschube, and E.F. Wieschaus. 2010.
958 Integration of contractile forces during tissue invagination. *J Cell Biol*. 188:735-749.

959 Martin, A.C., M. Kaschube, and E.F. Wieschaus. 2009. Pulsed contractions of an actin-myosin
960 network drive apical constriction. *Nature*. 457:495-499.
961 Mason, F.M., M. Tworoger, and A.C. Martin. 2013. Apical domain polarization localizes actin-
962 myosin activity to drive ratchet-like apical constriction. *Nat Cell Biol*. 15:926-936.
963 Mason, F.M., S. Xie, C.G. Vasquez, M. Tworoger, and A.C. Martin. 2016. RhoA GTPase
964 inhibition organizes contraction during epithelial morphogenesis. *J Cell Biol*. 214:603-
965 617.
966 Mitrossilis, D., J.C. Roper, D. Le Roy, B. Driquez, A. Michel, C. Menager, G. Shaw, S. Le
967 Denmat, L. Ranno, F. Dumas-Bouchiat, N.M. Dempsey, and E. Farge. 2017.
968 Mechanotransductive cascade of Myo-II-dependent mesoderm and endoderm
969 invaginations in embryo gastrulation. *Nat Commun*. 8:13883.
970 Mongera, A., P. Rowghanian, H.J. Gustafson, E. Shelton, D.A. Kealhofer, E.K. Carn, F.
971 Serwane, A.A. Lucio, J. Giammona, and O. Campas. 2018. A fluid-to-solid jamming
972 transition underlies vertebrate body axis elongation. *Nature*. 561:401-405.
973 Munjal, A., J.M. Philippe, E. Munro, and T. Lecuit. 2015. A self-organized biomechanical
974 network drives shape changes during tissue morphogenesis. *Nature*. 524:351-355.
975 Nikolaidou, K.K., and K. Barrett. 2004. A Rho GTPase signaling pathway is used reiteratively in
976 epithelial folding and potentially selects the outcome of Rho activation. *Curr Biol*.
977 14:1822-1826.
978 Oda, H., and S. Tsukita. 2001. Real-time imaging of cell-cell adherens junctions reveals that
979 Drosophila mesoderm invagination begins with two phases of apical constriction of cells.
980 *J. Cell Sci.* 114:493-501.
981 Perez-Mockus, G., K. Mazouni, V. Roca, G. Corradi, V. Conte, and F. Schweisguth. 2017.
982 Spatial regulation of contractility by Neuralized and Bearded during furrow invagination
983 in Drosophila. *Nat Commun*. 8:1594.
984 Priya, R., G.A. Gomez, S. Budnar, S. Verma, H.L. Cox, N.A. Hamilton, and A.S. Yap. 2015.
985 Feedback regulation through myosin II confers robustness on RhoA signalling at E-
986 cadherin junctions. *Nat Cell Biol*. 17:1282-1293.
987 Rahimi, N., I. Averbukh, S. Carmon, E.D. Schejter, N. Barkai, and B.Z. Shilo. 2019. Dynamics
988 of Spaetzle morphogen shuttling in the Drosophila embryo shapes pattern. *Development*.
989 146:doi: 10.1242/dev.181487.
990 Rauzi, M., U. Krzic, T.E. Saunders, M. Krajnc, P. Ziherl, L. Hufnagel, and M. Leptin. 2015.
991 Embryo-scale tissue mechanics during Drosophila gastrulation movements. *Nat Commun*.
992 6:8677.
993 Rembold, M., L. Ciglar, J.O. Yanez-Cuna, R.P. Zinzen, C. Girardot, A. Jain, M.A. Welte, A.
994 Stark, M. Leptin, and E.E. Furlong. 2014. A conserved role for Snail as a potentiator of
995 active transcription. *Genes Dev*. 28:167-181.
996 Rogers, K.W., and A.F. Schier. 2011. Morphogen gradients: from generation to interpretation.
997 *Annu Rev Cell Dev Biol*. 27:377-407.
998 Roth, S., D. Stein, and C. Nusslein-Volhard. 1989. A gradient of nuclear localization of the
999 dorsal protein determines dorsoventral pattern in the Drosophila embryo. *Cell*. 59:1189-
1000 1202.
1001 Rushlow, C.A., K. Han, J.L. Manley, and M. Levine. 1989. The graded distribution of the dorsal
1002 morphogen is initiated by selective nuclear transport in Drosophila. *Cell*. 59:1165-1177.
1003 Salbreux, G., G. Charras, and E. Paluch. 2012. Actin cortex mechanics and cellular
1004 morphogenesis. *Trends Cell Biol*. 22:536-545.

1005 Schindelin, J., I. Arganda-Carreras, E. Frise, V. Kaynig, M. Longair, T. Pietzsch, S. Preibisch, C.
1006 Rueden, S. Saalfeld, B. Schmid, J.Y. Tinevez, D.J. White, V. Hartenstein, K. Eliceiri, P.
1007 Tomancak, and A. Cardona. 2012. Fiji: an open-source platform for biological-image
1008 analysis. *Nat Methods*. 9:676-682.
1009 Simoes Sde, M., J.T. Blankenship, O. Weitz, D.L. Farrell, M. Tamada, R. Fernandez-Gonzalez,
1010 and J.A. Zallen. 2010. Rho-kinase directs Bazooka/Par-3 planar polarity during
1011 Drosophila axis elongation. *Dev Cell*. 19:377-388.
1012 Spahn, P., and R. Reuter. 2013. A vertex model of Drosophila ventral furrow formation. *PLoS*
1013 *One*. 8:e75051.
1014 Steward, R. 1989. Relocalization of the dorsal protein from the cytoplasm to the nucleus
1015 correlates with its function. *Cell*. 59:1179-1188.
1016 Steward, R., S.B. Zusman, L.H. Huang, and P. Schedl. 1988. The dorsal protein is distributed in
1017 a gradient in early Drosophila embryos. *Cell*. 55:487-495.
1018 Stricker, J., T. Falzone, and M.L. Gardel. 2010. Mechanics of the F-actin cytoskeleton. *J*
1019 *Biomech*. 43:9-14.
1020 Sui, L., S. Alt, M. Weigert, N. Dye, S. Eaton, F. Jug, E.W. Myers, F. Julicher, G. Salbreux, and
1021 C. Dahmann. 2018. Differential lateral and basal tension drive folding of Drosophila
1022 wing discs through two distinct mechanisms. *Nat Commun*. 9:4620.
1023 Sumigray, K.D., M. Terwilliger, and T. Lechler. 2018. Morphogenesis and
1024 Compartmentalization of the Intestinal Crypt. *Dev Cell*. 45:183-197 e185.
1025 Sweeton, D., S. Parks, M. Costa, and E. Wieschaus. 1991. Gastrulation in Drosophila: the
1026 formation of the ventral furrow and posterior midgut invaginations. *Development*.
1027 112:775-789.
1028 Thisse, B., C. Stoetzel, C. Gorostiza-Thisse, and F. Perrin-Schmitt. 1988. Sequence of the twist
1029 gene and nuclear localization of its protein in endomesodermal cells of early Drosophila
1030 embryos. *EMBO J*. 7:2175-2183.
1031 Ulrich, A., K.R. Andersen, and T.U. Schwartz. 2012. Exponential megapriming PCR (EMP)
1032 cloning--seamless DNA insertion into any target plasmid without sequence constraints.
1033 *PLoS One*. 7:e53360.
1034 Vasquez, C.G., M. Tworoger, and A.C. Martin. 2014. Dynamic myosin phosphorylation
1035 regulates contractile pulses and tissue integrity during epithelial morphogenesis. *J Cell*
1036 *Biol*. 206:435-450.
1037 von Dassow, M., and L.A. Davidson. 2009. Natural variation in embryo mechanics: gastrulation
1038 in Xenopus laevis is highly robust to variation in tissue stiffness. *Dev Dyn*. 238:2-18.
1039 Weng, M., and E. Wieschaus. 2016. Myosin-dependent remodeling of adherens junctions
1040 protects junctions from Snail-dependent disassembly. *J Cell Biol*. 212:219-229.
1041 Wolpert, L. 1969. Positional information and the spatial pattern of cellular differentiation. *J*
1042 *Theor Biol*. 25:1-47.
1043 Xie, S., and A.C. Martin. 2015. Intracellular signalling and intercellular coupling coordinate
1044 heterogeneous contractile events to facilitate tissue folding. *Nat Commun*. 6:7161.
1045 Yevick, H.G., P.W. Miller, J. Dunkel, and A.C. Martin. 2019. Structural Redundancy in
1046 Supracellular Actomyosin Networks Enables Robust Tissue Folding. *Dev Cell*. 50:586-
1047 598.
1048